

國立臺灣大學理學院海洋研究所



碩士論文

Institute of Oceanography

College of Science

National Taiwan University

Master Thesis

2018 年馬登-朱利安振盪(Madden-Julian Oscillation)活躍
期下風所引發之混合層加深

Wind-Induced Mixed Layer Deepening under the Active Phase of
Madden-Julian Oscillations (MJOs) in 2018

葉伏家

Fu-Chia Yeh

指導教授：許哲源 博士

Advisor: Je-Yuan Hsu, Ph.D.

中華民國 111 年 12 月

December 2022

國立臺灣大學碩士學位論文
口試委員會審定書

MASTER'S THESIS ACCEPTANCE CERTIFICATE
NATIONAL TAIWAN UNIVERSITY

2018 年馬登-朱利安振盪 (Madden-Julian Oscillation) 活躍期
下風所引發之混合層加深

Wind-Induced Mixed Layer Deepening under the Active Phase of
Madden-Julian Oscillations (MJOs) in 2018

本論文係葉伏家(R09241105)在國立臺灣大學海洋研究所完成之碩士學位論文，於民國 111 年 11 月 7 日承下列考試委員審查通過及口試及格，特此證明。


The undersigned, appointed by the Institute of Oceanography on 7 November, 2022 have examined a Master's thesis entitled above presented by Yeh Fu-Chia (R09241105) candidate and hereby certify that it is worthy of acceptance.

口試委員 Oral examination committee:

(指導教授 Advisor)


系主任/所長 Director: 謝志豪

致謝



時間很快來台大也超過兩年了，在海研所的期間，修了不少課也參與五次的航次，讓我對海洋更了解了許多，今天能完成論文，受到許多老師、同學們的幫助，其中最感謝的莫過於我的指導教授許哲源老師，從暑假一開始找老師就給我許多論文上的啟發，也循序漸進的帶領我了解論文所關注的議題與方向，這讓我學習到如何去思考物理海洋上的問題，與做一個研究的過程，研究過程中老師也給予我很大的彈性與自由規劃我自己的研究歷程，這都是我能在物理海洋學習的一大助力。此外也要感謝張明輝老師和鄭宇昕老師，在每周的 meeting 中總是能給我不同專業的觀點，讓我能從更多元的角度來討論我的研究，並最後擔任我的口試委員，也謝謝曾于恒老師在模式上給予的建議，碩一跟曾老師修的課十分受用。最後要謝謝清森跟芳瑜，雖然研界領域差比較多，但你們總是能抽空一起練習報告或分享研究生活大小事，能和你們一路從中山來台大當同學十分的幸運，我也會珍惜這段和你們一起學習的時光。

摘要



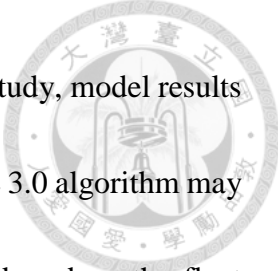
在北半球冬季，馬登-朱利安振盪 (MJO) 為季節內天氣系統具有顯著的深對流，從印度洋西部開始沿著赤道向東移動。2018 年 11 月在澳洲西北所佈放的兩個 EM-APEX floats、兩個 ALAMO floats 和一個 FIO buoy，測量 2018 年 12 月中旬 MJO 通過期間的海洋溫度、鹽度、水平流速與基本大氣參數。自 12 月 14 日以來，浮標量測到混合層在五天內從 25m 快速加深到 50m，並且該段時間內 MJO 所帶來的西風維持 9 ms^{-1} 以上，引起高達 0.4 ms^{-1} 的海流，破壞上層海洋的穩定。透過計算梯度理查森數(Ri)以發現不穩定性，由於經常觀測到小於 0.25 的 Ri，因此推測在強風作用下，上層海洋可能會出現不穩定和強烈的紊流混合。本研究使用 Thorpe scale 方法估算紊流耗散率，結果顯示混合層的紊流耗散率約為 10^{-7} Wkg^{-1} 至 10^{-6} Wkg^{-1} ，大於典型溫躍層內的紊流耗散率。在 MJO 連續幾天的風力作用下，剪切不穩定可能會發生強烈的紊流混合，從而使混合層加深。混合層加深導致海表溫度 (SST) 冷卻約 1.1°C ，SST 的變化改變了潛熱加顯熱量由 100 Wm^{-2} 增至 400 Wm^{-2} ，並有可能影響 MJO 的發展。由於混合層加深可能有助於海表冷卻，因此 MLD 變化在模式模擬中至關重要，研究中模式結果顯示，在 MJO 下使用 COARE 3.0 算法計算的風應力可能低估。因此通過觀測資料測量與估算正確風應力，可以在模式中更好地模擬 MJO 觀測的特徵，並進一步改進 MJO 的預報。

關鍵詞：馬登-朱利安振盪(MJO)、混合層加深、海表溫度冷卻、COARE 3.0、風應力

Abstract



During the boreal winter, Madden–Julian Oscillations (MJOs) as organized deep convections and intra-seasonal weather systems propagate eastward along the equator, starting from the west of the Indian Ocean. Two EM-APEX, two ALAMO floats, and an FIO buoy were deployed in the northwest coast of Australia, which captured the ocean responses of temperature, salinity, and horizontal current velocity during the passage of one MJO in the middle of December 2018. The four floats captured a rapid deepening of mixed layer depth (MLD) from 25 m to 50 m since 14th Dec in five days. At the same time, strong westerly wind associated with MJO was mostly $> 9 \text{ m s}^{-1}$. The wind-induced a strong current up to 0.4 m s^{-1} for destabilizing the upper ocean. The gradient Richardson number (Ri) was computed for identifying the instability. Because the low $\text{Ri} < 0.25$ was frequently observed, instability and strong turbulence might occur in the upper ocean under the strong wind forcing. Using the Thorpe-scale method, the turbulent dissipation rate was approximately 10^{-7} to $10^{-6} \text{ W kg}^{-1}$ in the MLD, which was larger than those within the typical thermocline. Strong turbulent mixing might occur via shear instability under the consecutive days of wind forcing, thereby MLD deepening. MLD deepening contributed to cooling sea surface temperature (SST) by about $1.1 \text{ }^\circ\text{C}$. The heat fluxes were modulated by SST variation from 100 to 400 W m^{-2} . The heat flux variation might affect the development of MJOs. Because MLD deepening may contribute to the cooling



of SST, the simulation of MLD variation is critical in models. In the study, model results demonstrate that the computation of the wind stress using the COARE 3.0 algorithm may be underestimated under MJO. Therefore, with correct wind stress based on the float measurements, several features of the observations can be better captured in models and further improve MJOs' forecasts.

Keywords: Madden–Julian Oscillations, Mixed layer deepening, SST cooling, COARE 3.0 algorithm, wind stress.

Content



致謝.....	i
摘要.....	ii
Abstract.....	iii
Content	v
List of Figures.....	viii
List of Tables	xiii
1 Introduction	1
2 Measurements under the MJO in 2018.....	4
2.1 Profiling floats and buoy measurement.....	4
2.2 Other datasets in the study.....	7
2.3 Madden-Julian Oscillation in 2018	8
3 Upper ocean structure and atmosphere responses to the MJO	11
3.1 Surface wind, ocean responses, and SST cooling	11
3.1.1 Surface wind on the buoy	11
3.1.2 Upper ocean structure.....	12
3.1.3 Current velocity.....	15
3.2 Heat fluxed variations.....	16
3.3 Summary to MJO in 2018	17



4	Wind-induce mixed layer deepening	19
4.1	Mixed layer depth deepening	19
4.2	Gradient Richardson number	21
4.3	Thorpe scale method and dissipation rate	23
4.4	Summary of mixed layer depth deepening	25
5	Effect of Turbulent Mixing under MJOs	26
5.1	Model description	26
5.2	Simulating mixed layer depth deepening	28
5.3	Effects on vertical resolution in the upper ocean	29
5.4	Parameters in the KPP mixing scheme	31
5.5	Summary of MLD simulation by using KPP	33
6	Momentum and Buoyancy Response during MJOs	35
6.1	Wind drag coefficient	36
6.2	Wind-induce current	37
6.3	Linear momentum budget method and wind stress	40
6.3.1	Linear momentum budget method	40
6.3.2	Wind stress	41
6.4	Buoyancy flux effect	45
7	Conclusion and discussion	47

Reference51





List of Figures

- Fig. 1: The trajectories of AL9207 (black), AL9209 (cyan), EM8487 (green), and EM8488 (purple) from 11th Dec to 21st Dec 2018. The position of the FIO buoy is displayed as a white point. Geostrophic current (black arrows) derived Sea surface height anomalies (shading) from NOAA altimetry data of 14th Dec..... 6
- Fig. 2: (a) Daily OLR anomalies from NOAA and (b) TRMM precipitation rates averaged over 10°S–10°N from 50°E–130°E during Oct–Dec 2018. The dashed lines are the location longitude of the buoy. (c) Mean OLR and Mean precipitation rates averaged over 10°S–10°N at 115.1°E..... 9
- Fig. 3: RMM1 and RMM2 index through 8 different areas. The index outside this center circle is regarded as an MJO moving from west to east. Contrastingly, MJO is considered weak when this is within the center circle. 10
- Fig. 4: (a) Wind speed at 4 m height on the buoy above the sea surface (b) east-west component (c) north-south component of wind speed. 12
- Fig. 5: Temperature profiles of (a) AL9207, (c) AL9209, (d) EM8487, and (g) EM8488. Salinity of (b) AL9207, (d) AL9209, (f) EM848, and (h) EM8488. 14
- Fig. 6: (a) SST of AL9207 (blue line) and AL9209 (orange line) and (b) Himawari-8 satellite measurements of skin-SST at AL9207 (blue line), AL9209 (orange line) and EM8487 (green), and EM8488 (magenta)..... 15



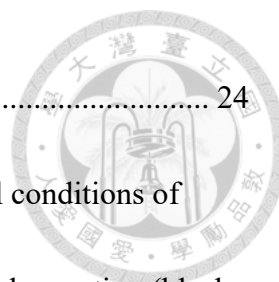
Fig. 7: (a) East-west components and (b) north-south components of measurements of current velocity taken by EM8487. (c) East-west and (d) north-south components of measurements of current velocity taken by EM8488. The missing data are expressed with gray dots. 16

Fig. 8: (a) Latent heat plus sensible heat flux (orange line: AL9207; green line: AL9209). (b) Shortwave radiation (yellow line) and longwave radiation (pink line) on buoy. (c) Surface air temperature (blue line), and SST (orange line: AL9207; green line: AL9209) (d) Relative humidity on buoy measurement. 18

Fig. 9: (a)–(d) Surface MLD (magenta lines) and buoyancy frequency N^2 (shading) derived from two ALAMO floats and two EM-APEX floats measurements AL9207, AL9209, EM8487, and EM8488, respectively. The negative values of N^2 are expressed with pink dots. The missing data are expressed with gray dots. 20

Fig. 10: (a) and (d) are the buoyancy stratification N^2 (shading) derived from EM8487 and EM8488. The negative values of N^2 are expressed with pink dots. (b) and (e) are vertical shear square of EM8487 and EM8488 (c) and (f) are $(1/Ri) - 4$ and surface MLD (black lines) of EM8487 and EM8488. The missing data are expressed with gray dots. 22

Fig. 11: (a) and (b) are TKE dissipation rate and MLD (black lines) estimated by Thorpe scale method. The value below 10^{-11} are denoted with gray dots. (c) and (d) are



($1/Ri$) – 4 and surface MLD (black lines)..... 24

Fig. 12: (a)–(c) Simulations of MLD deepening at the different initial conditions of three floats in KPP (blue line), with the comparison to the float observation (black line)..... 29

Fig. 13: Different vertical resolutions on simulations of MLD (a)–(c) at AL9207, AL9209, and EM8487 (blue: 4 m; orange: 2 m; yellow: 1 m), with the comparison to the float observation (black line)..... 30

Fig. 14: Different gradient Richardson number on simulations of MLD (a)–(c) at AL9207, AL9209 and EM8487 (blue: $Ri_0 = 0.4$; orange: $Ri_0 = 0.7$; yellow: $Ri_0 = 1$), with the comparison to the float observation (black line)..... 32

Fig. 15: Different bulk Richardson number on simulations of MLD (a)–(c) at AL9207, AL9209 and EM8487 (blue: $Ri_c = 0.3$; orange: $Ri_c = 0.5$; yellow: $Ri_c = 0.7$), with the comparison to the float observation (black line). 33

Fig. 16: Current velocity averaged from 0 m to 20 m depth of EM8487 (blue line) and ROMS (orange line). 35

Fig. 17: Different magnitude of wind stress on simulations of MLD (a)–(c) at AL9207, AL9209 and EM8487, (blue: wind stress estimated from COARE 3.0; orange: 1.2 times; yellow: 1.5 times; purple: 1.8 times of wind stress), with the float observation (black line). 37

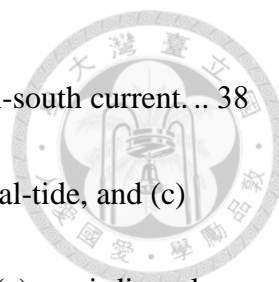


Fig. 18: Power spectrum density of (a) east-west current and (b) north-south current. ... 38

Fig. 19: East-west components of (a) current velocity, (b) semi-diurnal-tide, and (c) inertial current; north-south components of (d) current velocity (e) semi-diurnal-tide, and (f) inertial current. The missing data are expressed with gray dots. 39

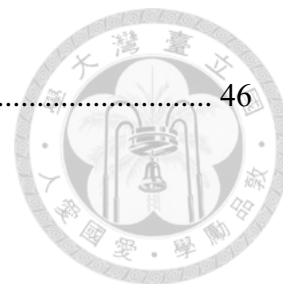
Fig. 20: (a) East-west and (b) north-south component of EM8487 measurement excluding semi-diurnal tides and background current (c) East-west and (d) north-south component of ROMS results which have been adjusted with time lags. 40

Fig. 21. Depth-integrated comparisons of float observations (black line with one standard deviation error bars) and KPP simulations (orange: COARE 3.0 estimated; blue: 1.5 times; green: 1.8 times of wind stress) during the MJO. (a) and (c) is the time rate change momentum of U and V components, respectively. (b) and (d) is Coriolis force terms of U and V components, respectively. 44

Fig. 22: The drag coefficient C_d as a function of wind speed at 10 m above the sea (yellow: Large and Pond, 1981; green: COARE 3.0 estimated; blue: derived from observation; orange: derived from 1.35 times of wind with one standard deviation error bars) 44

Fig. 23: The heat flux input in MLD simulation of COARE 3.0 estimated (blue line); estimated value + 50 W m^{-2} (orange line); estimated value - 50 W m^{-2} (yellow line) compare to the float observation (black line) at (a)–(c) at AL9207, AL9209 and

EM8487.....46



List of Tables

Tab. 1: Floats measured properties and resolution. 7

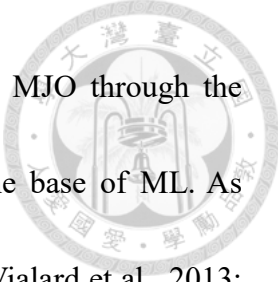




1 Introduction


Madden-Julian oscillations (MJO, Madden & Julian, 1972), an intraseasonal planetary-scale weather system, propagate eastward through the tropical warm pool. MJO convection typically consists of large-scale coupled patterns in atmospheric circulation associated with surface westerly wind bursts and heavy precipitation (Zhang 2005). Strong oceanic responses to the westerly wind bursts result in a cooling of the ocean mixed layer and SST (Hendon et al., 1998; Vialard et al., 2008; Moum et al., 2014). Several model studies have illustrated that air-sea heat and moisture fluxes can be modeled significantly by upper ocean structure and SST variation. The change of air-sea heat and moisture fluxes involve the MJOs convection evolution and propagation (Bernie et al., 2008; DeMott et al. 2015; Ruppert and Johnson, 2015). Owing to this, exploring the interaction between atmospheric features of MJOs and the upper ocean responses can aid the model prediction on intraseasonal weather systems.

The ocean mixed layer (ML) is commonly considered the layer from the sea surface to the top of the seasonal thermocline where features vertically quasi-homogeneous in temperature or density due to well mixed by turbulence (Kara et al., 2000, Lorbacher et al., 2006). Surface mixed layer depth (MLD) is important in the heat budget because it determines heat content and the water column to which net surface heat flux is distributed.



(Chen et al., 1994). The temperature within MLD decrease during MJO through the entrain of colder water, which is caused by turbulent mixing at the base of ML. As previous studies and observations in the stratified ocean suggested (Vialard et al., 2013; Moum et al., 2014; Marshall and Hendon, 2014), the shear of horizontal current due to direct wind influences is the principal factor for rapid upper ocean cooling, while the wind is effective. Because significant westerly wind bursts often occur during the active phase of MJOs, studying the effect of wind is critical for understanding the momentum transported into the ocean in the MJO-ocean interaction.

Note that the westerly wind associated with the MJO (Wyrтки, 1973; Nagura and McPhaden, 2008; Schott et al., 2009) may generate significant vertical shear in the surface mixed layer. Once the ratio of buoyancy frequency squared to vertical shear squared, i.e., the gradient Richardson number, is less than 0.25, it may induce the shear instability (Miles and Howard, 1961). Strong turbulence due to the shear instability may then destabilize the stratified oceans to deepen the surface mixed layer (Yusuke Ushijima et al., 2020). Model studies on the wind-driven deepening of ML demonstrate the factors regarding turbulence process, which include buoyancy and energy source to vertical shear for instability (Price et al., 1986; Large et al., 1994). Thus, quantitating the MLD deepening rate as well as the momentum transport into the ocean is essential to better understanding and simulating such upper ocean processes on MJOs.



In November 2018, the Centre for Southern Hemisphere Oceans Research (CSHOR) and China's First Institution of Oceanography conducted a collaborative field campaign to explore the air-sea interaction in the Indonesian Australian Basin (Feng et al. 2020).

The observations of an MJO event were documented in this study. The surface wind speed was measured up to 10 m s^{-1} during the MJO active phase. At the same time, the MLD deepened rapidly from 25 to 50 m in five days, which is more rapidly than the response to the mature stage of the Indian summer monsoon (Liu et al., 2021). In the first two days following the arrival of MJO, the SST was cooling $> 1 \text{ }^{\circ}\text{C}$. Because the temperature between SST and air temperature rose, the heat flux into the ocean is increased to 400 W m^{-2} . In the following, the observations and data will be described in section 2. The upper ocean responses and flux variation between air-sea is discussed in section 3. Then, the dynamic of MLD deepening will be presented in Section 4. The comparison of the observations with the model results using the K-profile parameterization (KPP) as well as the momentum budget estimated will be highlighted in Sections 5 and 6, respectively.

2 Measurements under the MJO in 2018



2.1 Profiling floats and buoy measurement

Six Air Launched Autonomous Micro Observer (ALOMO, AL9205, AL9206, AL9207, AL9208, AL9209, AL9210) profiling floats and two Electromagnetic Autonomous Profiling Explorer (EM-APEX, EM8487 and EM8488) floats were deployed at 115.3 °E and 16.8 °S on 22nd Nov, 2018 (Feng et al. 2020). Four floats (AL9207, AL9209, EM8487 and EM8488) remained and profiled the upper ocean structure until the middle of December. An anti-cyclonic eddy trapped the floats during December, 2018. AL9207, AL9209, and EM8487 were located in the south and drifted eastward; whereas the EM8488 was situated on the east side and drifted northward (Fig. 1). A mini-version of the Bailong buoy system from the FIO lab (Cole et al. 2011) was deployed at 16.5°S, 115.1°E on 21st Nov (Fig. 1). This Bailong buoy system was engaged in measuring the surface air temperature, pressure, humidity, surface winds, shortwave and longwave radiations at 10 min intervals. With satellites, the real-time data which recorded from the buoy were transmitted to the FIO lab. The wind is ~ 5 to 6 m s⁻¹ from 14th to 17th Dec 2018.

The two ALOMO floats and two EM-APEX floats were equipped with different types of CTD sensors (SBE-41 on AL9207, EM8487, EM8488 and RBR on AL9209),

making the discrepancy on vertical and temporal resolution, as well as the SST estimating.

AL9207 and AL9209 profiled from sea surface down to 300 m and 500 m, respectively.

EM8487 and EM8488 profiled from about from 10 m to 300m. The vertical resolution of

temperature and salinity on SBE-41 mounted on ALOMO floats (AL9207) and EM-

APEX (EM8487, EM8488) was 1 m and 3.5 m, respectively. For the CTD measurements

taken by the RBR at AL9209, the vertical resolution was 0.1 m in the upper 5 m and 1 m

below 5 m. ALOMO floats profiled during the ascending phase, and the temporal

resolution between each profile is 8 h at AL9207 and 3 h at AL9209 (Feng et al. 2020).

EM-APEX profiled during ascending and descending phases. The temporal resolution of

a cycle of ascending and descending was 2 hours. (Sanford et al., 2005; Hsu et al., 2017).

For the estimation of SST, ALAMO floats record the temperature during ascending,

corresponding to the measured pressure less than 0.2 dbar. Because the SBE-41 CTD

sensor at AL9207 did not measure in the upper 1 m, after the float entered the mission of

surface phase, the first value of temperature measurements at about 0.1 or 0.2 bar was

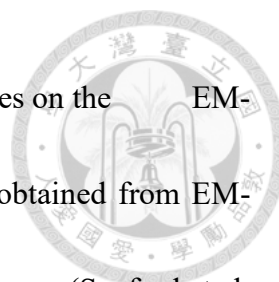
used as SST. The estimated SST was several degrees higher than those at pressures < 0

dbar, similar to the typical difference between the SST and air temperature in the region

(Hsu et.al 2022). On the AL9209, SST was found by the highest temperature where at

around 0.2 m depth in the upper 1 m, after excluding air temperature which salinity

measurements were < 32 psu in the samples.



Except temperature and salinity, two orthogonal pairs of electrodes on the EM-APEX floats can measure the voltage. The horizontal current was obtained from EM-APEX floats which measured the electric and magnetic fields in the ocean (Sanford et al. 2005). The electromagnetic currents, induced by seawater motion, is measured and used to estimate the oceanic current velocity based on the principle of motional induction (Sanford et al. 1978). The vertical resolution of horizontal current velocity was around 3.1 m.

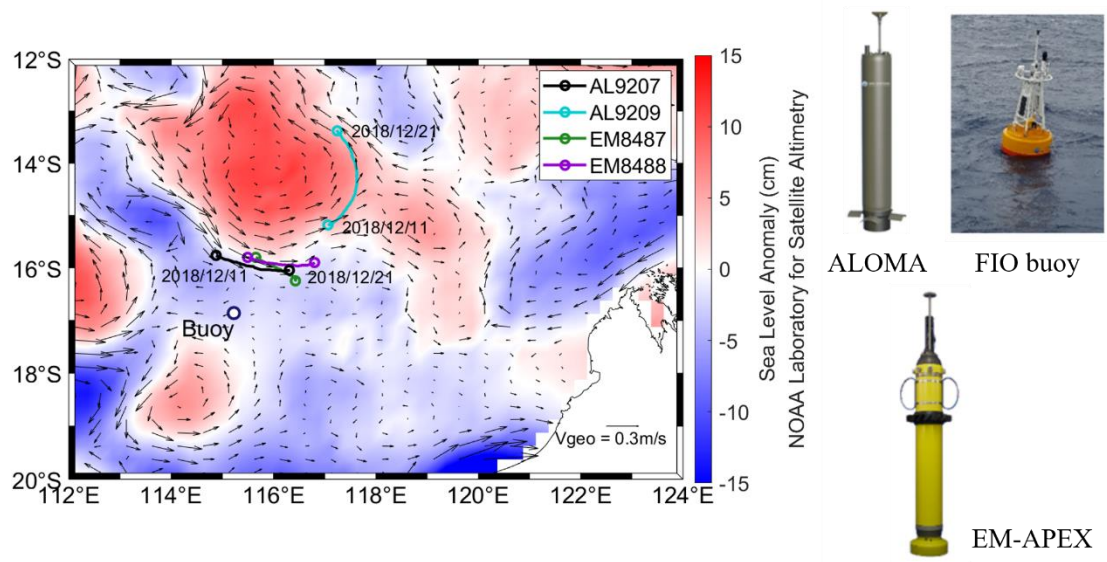
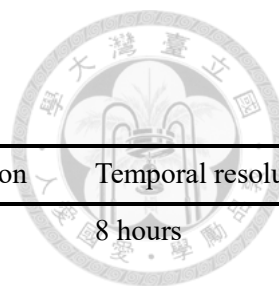


Fig. 1: The trajectories of AL9207 (black), AL9209 (cyan), EM8487 (green), and EM8488 (purple) from 11th Dec to 21st Dec 2018. The position of the FIO buoy is displayed as a white point. Geostrophic current (black arrows) derived Sea surface height anomalies (shading) from NOAA altimetry data of 14th Dec.



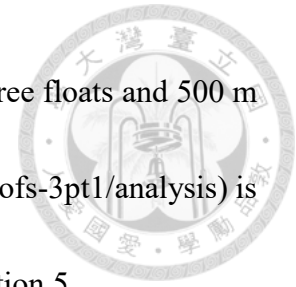
Tab. 1: Floats measured properties and resolution.

Float name	Measurements	Profiling depth	Vertical resolution	Temporal resolution
AL9207	Temperature, Salinity	500 m	1 m	8 hours
AL9209	Temperature, Salinity	350m	Upper 5 m: 0.1 m Below 5 m: 1 m	3 hours
EM8487	Temperature, Salinity, current velocity	10m-300m	CTD: 3.5 m Current: 3.1 m	~2 hour
EM8488	Temperature, Salinity, current velocity	10m-300m	CTD: 3.5 m Current: 3.2 m	~2 hour

2.2 Other datasets in the study

Several other datasets are utilized for describing atmospheric and oceanic states during the passage of the MJO. The satellite altimetry data is provided by the NOAA Laboratory, which can be used for computing the geostrophic current. Daily outgoing longwave radiation (OLR) data from NOAA (<https://psl.noaa.gov>) and precipitation data from the near-real-time legacy product of Tropical Rainfall Measuring Mission (TRMM) Multi satellite Precipitation Analysis (Huffman and Bolvin 2018) is used to identify the propagation of MJO convection. The fifth generation European Centre for Medium-Range Weather Forecasts (ECMWF) reanalysis (ERA5; Hersbach et al. 2020) with horizontal resolution of $0.25^\circ \times 0.25^\circ$ is used to compare the atmosphere data measured by the buoy. Himawari-8 satellite measurements of SST were used to compare with the SST on floats (<https://registry.opendata.aws/noaa-himawari>). Because the floats only

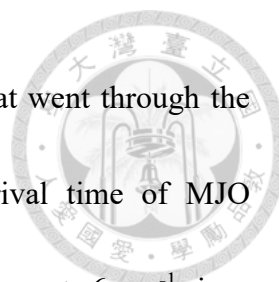
profile the temperature and salinity in the upper around 300 m on three floats and 500 m on a float, HYCOM GOFS 3.1 (<https://www.hycom.org/dataserver/gofs-3pt1/analysis>) is used for the initial condition of deep ocean in the model's run in section 5.



2.3 Madden-Julian Oscillation in 2018

The MJO active phase is characterized with the presence of a deep convective anomaly (Wheeler and Hendon 2004). Therefore, the remote-sensing measurements of precipitation and outgoing longwave radiation (OLR) from 10 °N to 10 °S are used to identify the convective events due to the MJOs. The anomalies with the eastward propagation of the convective systems are regarded as activate phase of MJO events (Fig. 2). We also use the RMM1 and RMM2 indexes (Real-time Multivariate MJO series 1, 2; Wheeler and Hendon, 2004), provided by Australia Bureau Meteorology (BoM), to describe the evolution of the MJO along the equator. RMM1 and RMM2 are mathematical methods which combine cloud amount and winds at upper and lower levels of the atmosphere. The index provides MJO strength and location in 8 different areas (Fig. 3).

In the middle of December, an eastward propagating signal arrived at the longitude of the buoy and floats. Despite the rain did not increase significantly, the mean OLR which was from 10 °N to 10 °S, started to decline from 230 W m⁻² to 190 W m⁻² on 14th Dec. Meanwhile, the RMM1 and RMM2, which combined cloud amounts and winds at



upper and lower atmosphere levels, demonstrated an MJO event that went through the north of Australia (<http://www.bom.gov.au/climate/mjo/>). The arrival time of MJO convection explained why the wind speed measurements at the buoy were $> 6 \text{ m s}^{-1}$ since 14th Dec. Therefore, these five days were defined as the MJO activity phase in the study.

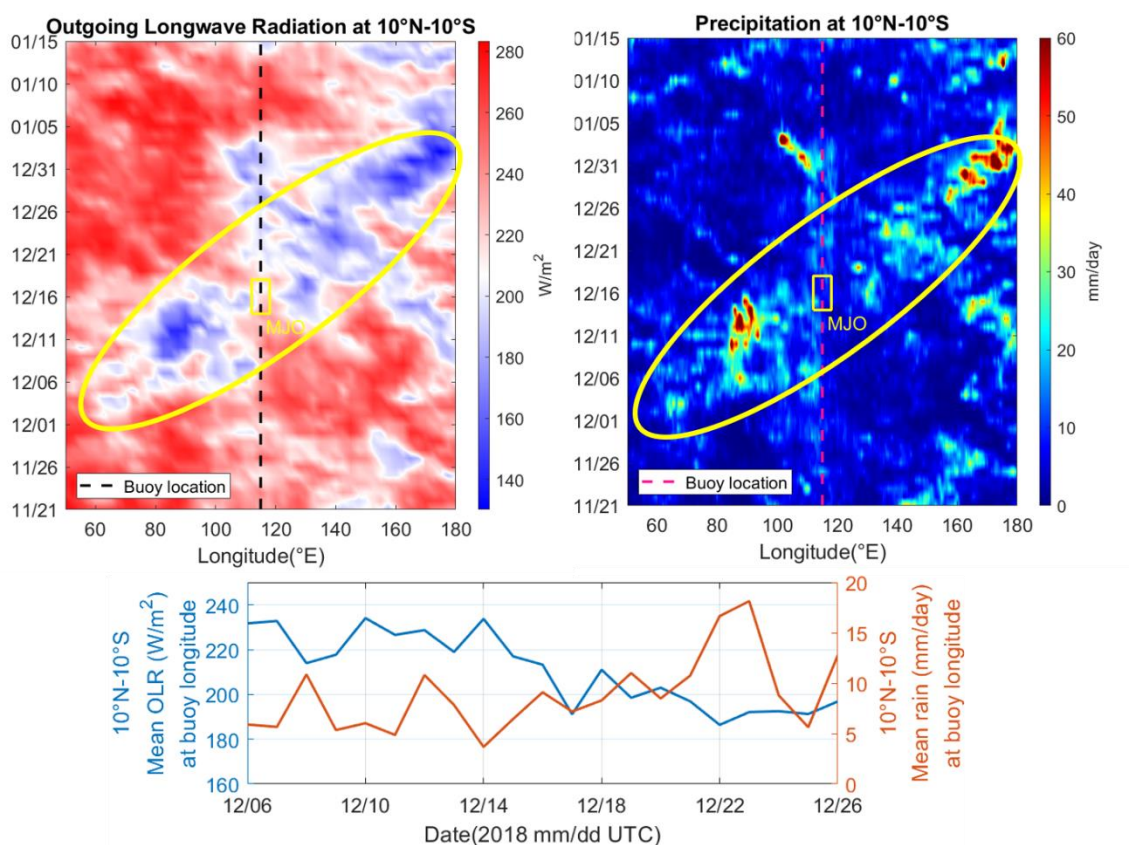


Fig. 2: (a) Daily OLR anomalies from NOAA and (b) TRMM precipitation rates averaged over 10°S–10°N from 50°E–130°E during Oct–Dec 2018. The dashed lines are the location longitude of the buoy. (c) Mean OLR and Mean precipitation rates averaged over 10°S–10°N at 115.1°E.

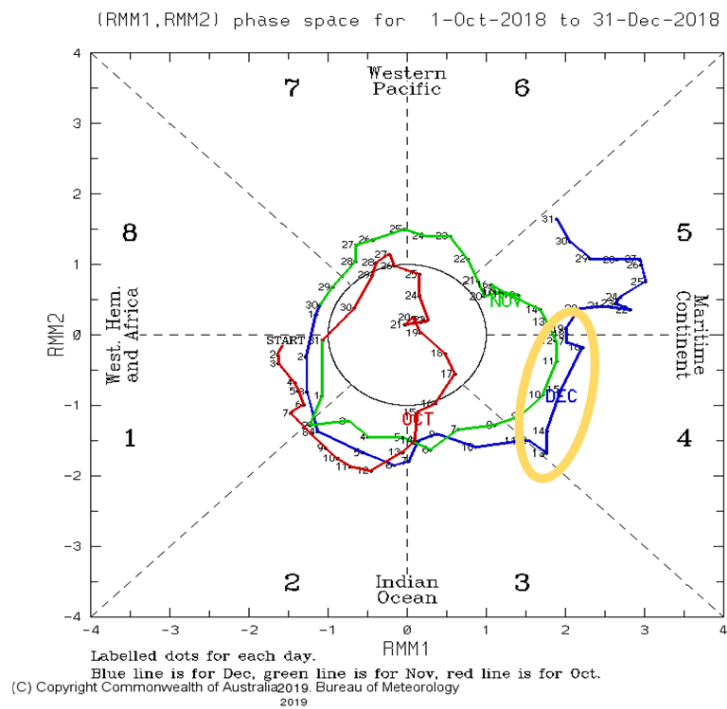


Fig. 3: RMM1 and RMM2 index through 8 different areas. The index outside this center circle is regarded as an MJO moving from west to east. Contrastingly, MJO is considered weak when this is within the center circle.



3 Upper ocean structure and atmosphere responses to the

MJO

Based on satellite data, MJO passed the location of floats and buoy from 14th to 17th Dec 2018. During the MJO passage, ocean temperature, salinity, current velocity profiles, and several atmosphere parameters were recorded. Below, we will use these data sets to explore the upper ocean response to the MJO and corresponding oceanic feedback to the MJO's deep convection.

3.1 Surface wind, ocean responses, and SST cooling

3.1.1 Surface wind on the buoy

During the MJO active phase, the wind direction was mainly toward northeast (Fig. 4), and consistent with the ECMWF wind data. The wind speed increased up to around 10 m s^{-1} when MJO convection arrived. The meridional wind did not change significantly in the MJO period and maintained about 6 m s^{-1} . On the other hand, the westerly wind increased from approximately 3 m s^{-1} to 6 m s^{-1} from 12th Dec to 14th Dec. The wind speed is ~ 5 to 6 m s^{-1} until the end of MJO. The increasing wind may enhance the mixing in the upper ocean.

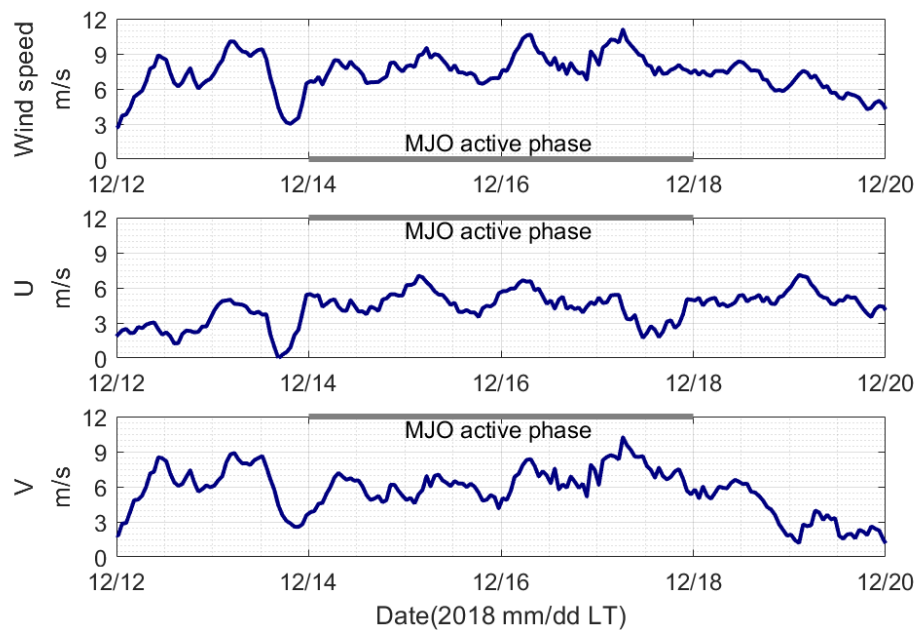
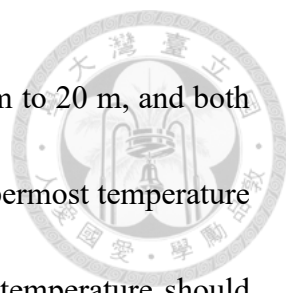


Fig. 4: (a) Wind speed at 4 m height on the buoy above the sea surface (b) east-west component (c) north-south component of wind speed.

3.1.2 Upper ocean structure

The float measurements were used for exploring the upper ocean response to the MJO. The temperature in the upper 20 m of three floats was greater than 28 °C from 13th to 14th Dec 2018 before the MJO and generated a warm layer. When the MJO convection arrived at the float positions, the temperature dropping was found with the four floats in the upper 20 m and extended to the upper 40 m due to the vertically mixed (Fig. 5). The mean temperature in the upper 20 m decreased by 1.0 °C in three days at AL9207 and AL9209. It was similar to the change of the SST, cooled by about 1.0 °C (AL9207) and 1.2 °C (AL9209) within the same period. Because EM8487 and EM8488 did not measure



the temperature above 15 m, the temperature was averaged from 15m to 20 m, and both values were 0.5 °C drop in the same period. Since the SST is the uppermost temperature of the ocean layers, the SST cooling and decrease of upper-ocean temperature should result from the entrainment of colder water below the mixed layer during the MJO. Studying dynamics for inducing the entrainment of cold water during the MJO active phase is crucial.

On the other hand, the salinity was around 34.5 psu in the upper 30 m at AL9207 and EM8487, which was 0.1 higher than AL9209 on 14th Dec when MJO arrived. In the following five days, the salinity increased by about 0.5 psu. At EM8488, the salinity was homogenous about 34.4 psu in the upper 50 m during the concerned period. The decrease in salinity might be caused by rising evaporation due to the increase in wind speed. On these four floats, a lower salinity layer was found within 40 m to 60 m, and the difference came by 0.15 psu with the upper layer. These led to a strong stratification at that depth.

Besides the floats measurements for exploring the vertical change of upper ocean structure, satellite data were also used to discuss the spatial variations of SST cooling (Fig. 6). The spatial variation of skin SST data were obtained from Himawari-8 satellite measurements, which removed the low-quality data and averaged the nearest eight data points ($0.5^{\circ} \times 0.5^{\circ}$ region) from the float position. The comparison demonstrated that the skin SST had the same cooling trend than the floats' SST, despite it was 2 °C larger than



floats. Therefore, even the SST measurement at the floats was the sea state at the single points, the change of SST was still consistent with the general trend of SST within this region. The skin-SST of EM8488 was around 1 °C higher than the other floats in that EM8488 was located farther north than the others (Fig. 1).

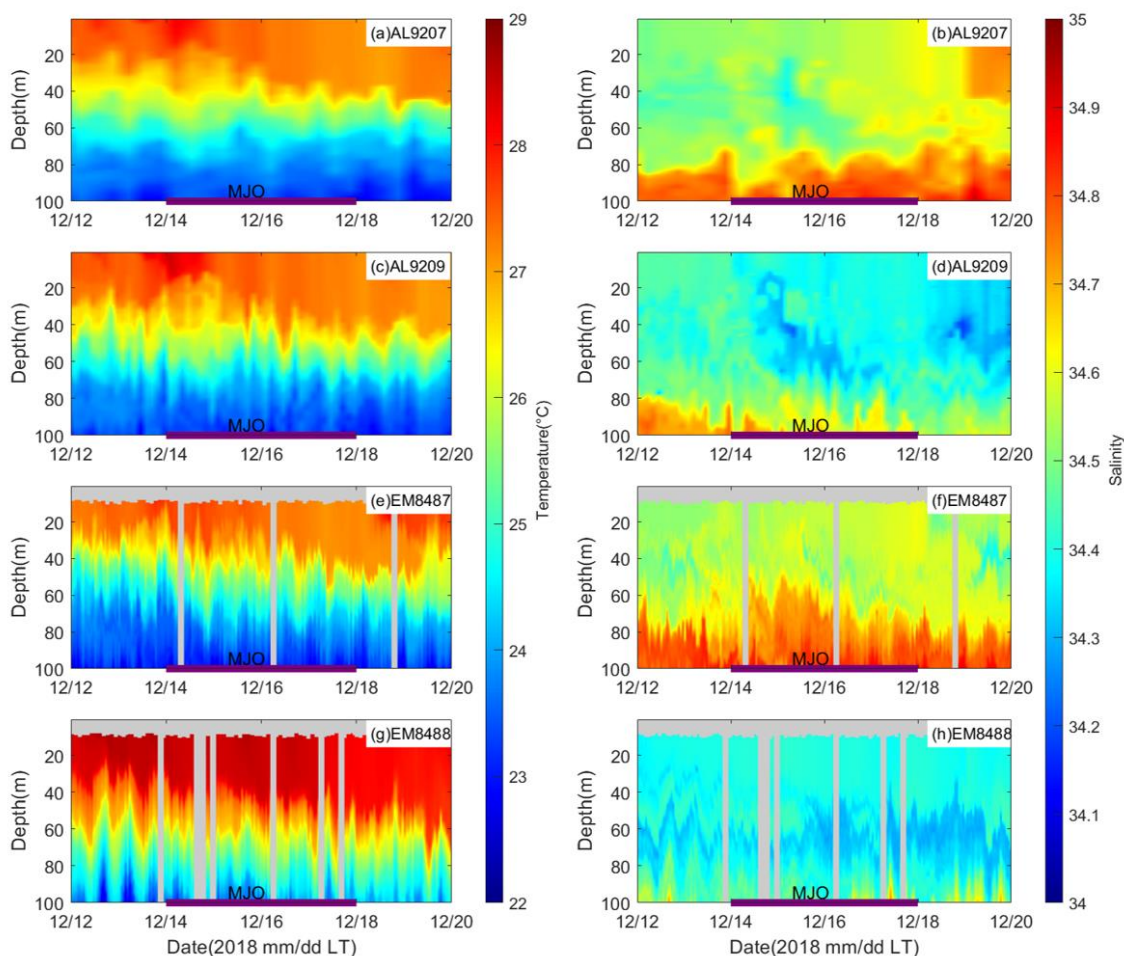


Fig. 5: Temperature profiles of (a) AL9207, (c) AL9209, (d) EM8487, and (g) EM8488. Salinity of (b) AL9207, (d) AL9209, (f) EM848, and (h) EM8488.

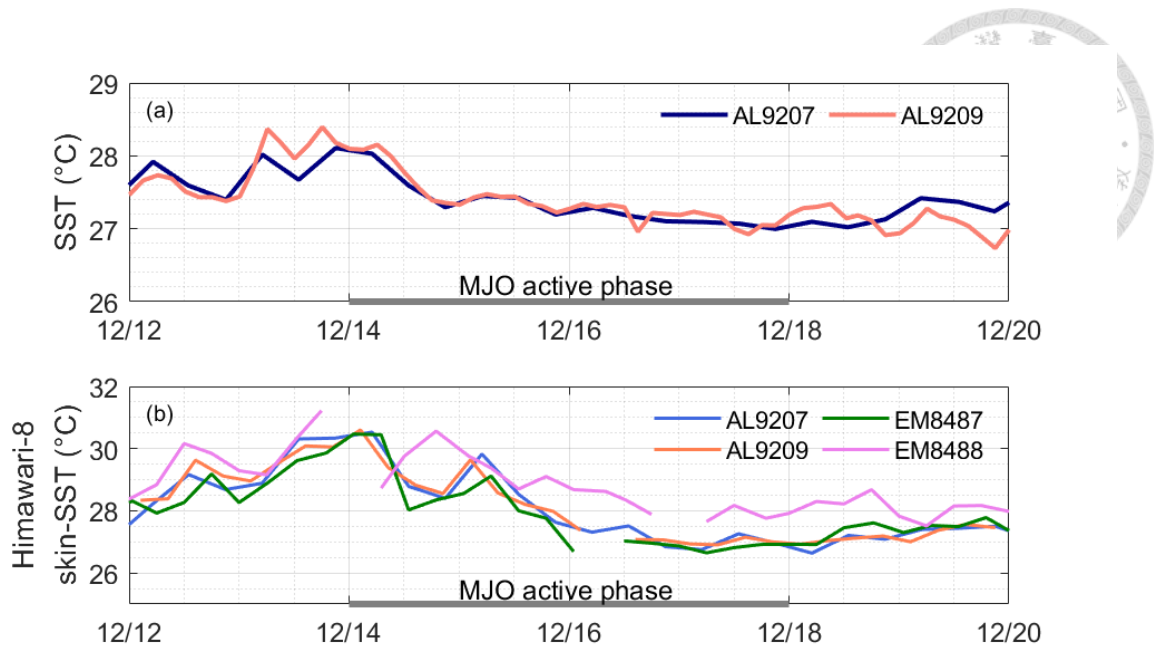


Fig. 6: (a) SST of AL9207 (blue line) and AL9209 (orange line) and (b) Himawari-8 satellite measurements of skin-SST at AL9207 (blue line), AL9209 (orange line) and EM8487 (green), and EM8488 (magenta).

3.1.3 Current velocity

Horizontal current velocity was measured from EM8487 and EM8488, which provided information on current magnitude and variation under the MJO westerly wind (Fig. 7). Before the passage of MJO's deep convection, horizontal current at EM8747 was less than 0.2 m s^{-1} in the upper 100 m. When the MJO convections arrived, the eastward current accelerated to 0.4 m s^{-1} in the upper 60 m, whereas north-south did not change apparently. The accelerated eastward current might be caused by the strong westerly wind (Fig. 4). It might induce strong vertical shear of horizontal current and vertical mixing via shear instability mixing. On EM8488 east-west current decreased from 0.2 m s^{-1} to -0.1



$m\ s^{-1}$, consistent with the variation of the magnitude of geostrophic current from sea surface height anomalies (Fig. 1).

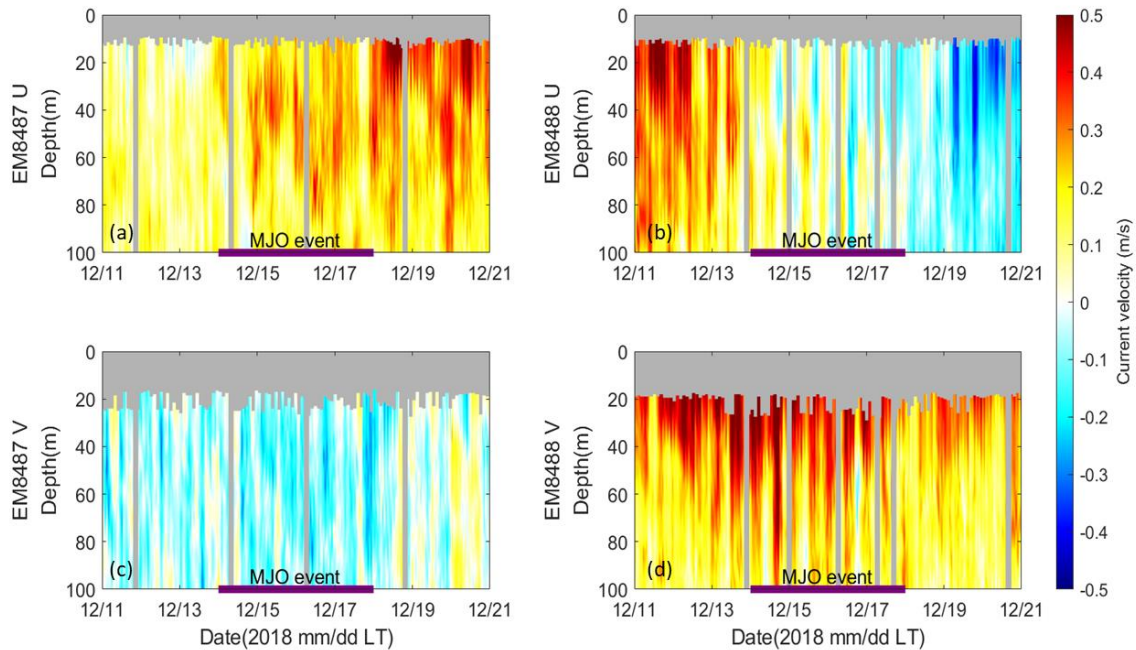



Fig. 7: (a) East-west components and (b) north-south components of measurements of current velocity taken by EM8487. (c) East-west and (d) north-south components of measurements of current velocity taken by EM8488. The missing data are expressed with gray dots.

3.2 Heat fluxed variations

Air-sea heat fluxes were computed by using the atmospheric measurements from the buoy and float measured SST, based on the COARE 3.5 algorithm (Fairall et al. 1996a; Fairall et al. 2003) (Fig. 8). Because the SST was cooled by $1.1\ ^\circ\text{C}$ in three days, the difference between air temperature and SST increased from 1 to $2.5\ ^\circ\text{C}$ during the active



phase. The increase of wind speed can also favor the evaporation, thereby latent heat changing. Additionally, the dry southerly winds from the Australian continent might influence the humidity drop at the air-sea interface from 16th to 20th Dec (Feng et al. 2020). The decline in humidity also favored the evaporation. The latent (LH) plus sensible heat flux (SH) therefore rose from 100 to 400 W m⁻² between 14th and 18th Dec. The downward shortwave radiation decreased by about 50 W m⁻² on 13th Dec and 16th Dec. The flux variation affected the convection development. During the MJO active phase, SST cooling caused by probable vertical mixing resulted in heat flux variation, which affected convection development. In other words, the dynamics that control the SST change magnitude in the upper ocean are essential in MJO evolution.

3.3 Summary to MJO in 2018

During the MJO convection from 14th to 18th Dec, a buoy, two ALAMO floats, and two EM-EPAX floats recorded the ocean and atmosphere variations. After the arrival of MJO convection to the floats, the wind raised to 10 m s⁻¹. The horizontal current increased 0.4 m s⁻¹ at EM8487 in upper 40 m simultaneously. The stronger current might destabilize ocean stratification via shear instability. As a result, the colder water below entrained to the mixed layer, resulting in the upper ocean and SST cooling at about 1.1 °C. The heat flux was modified from 100 W m⁻² to 400 W m⁻² by the SST variation and might

significantly affect the convection system development.

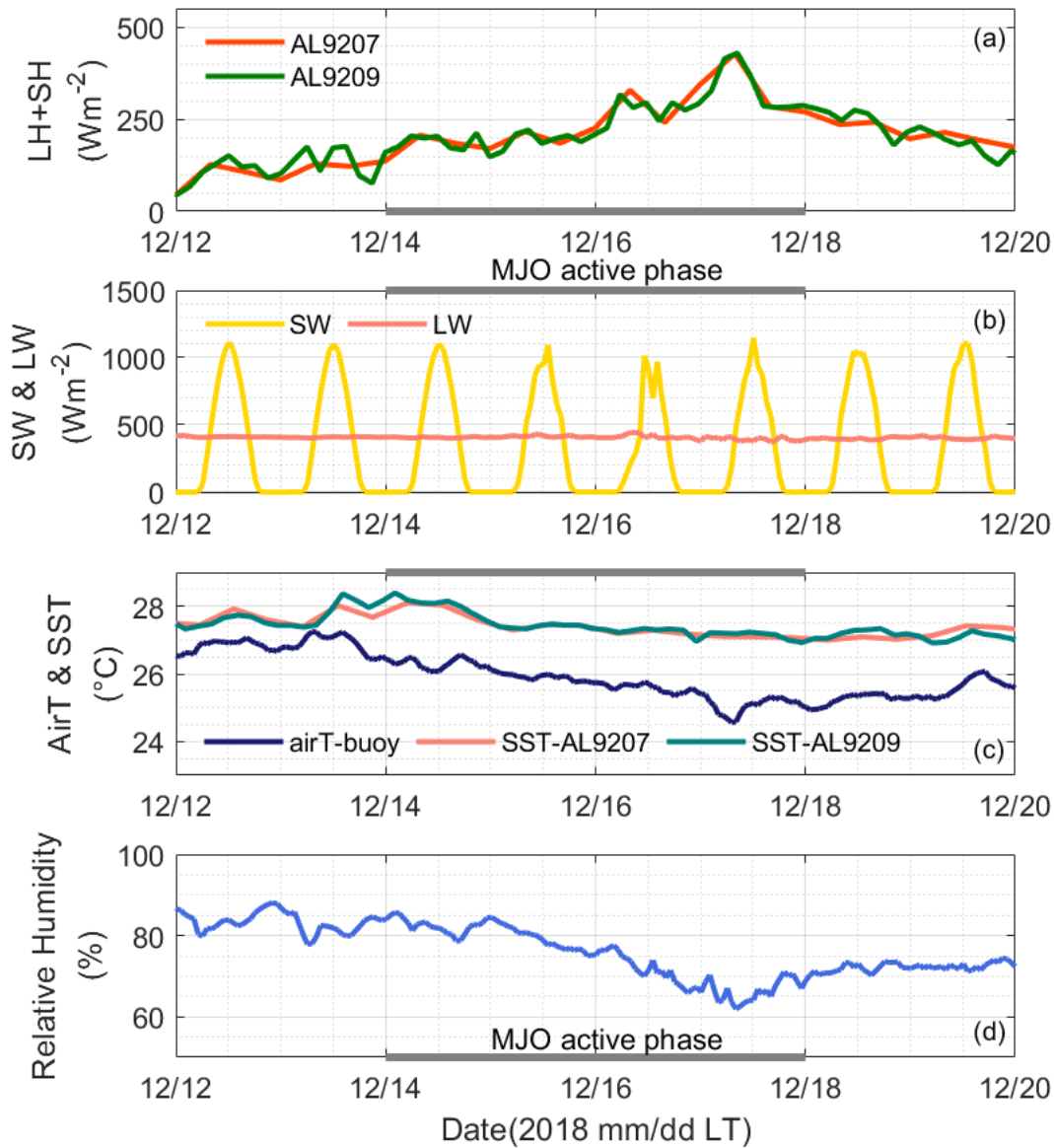


Fig. 8: (a) Latent heat plus sensible heat flux (orange line: AL9207; green line: AL9209).

(b) Shortwave radiation (yellow line) and longwave radiation (pink line) on buoy. (c)

Surface air temperature (blue line), and SST (orange line: AL9207; green line: AL9209)

(d) Relative humidity on buoy measurement.

4 Wind-Induce mixed layer deepening



Based on the buoy and floats measurement, the increase of wind and the acceleration of horizontal current in the upper 40 m occur simultaneously. The stronger current may destabilize ocean stratification via shear instability. This section will therefore explore factors for causing the change in surface MLD.

4.1 Mixed layer depth deepening

Multiple MLD criteria are proposed, including temperature and density-based criteria such as temperature difference near the ocean surface (Wyrki 1964) or density gradient criteria (Lukas and Lindstrom 1991). Here, we compute the MLD by exploring the difference of potential density between MLD and reference depth z_0 that exceed a constant. The z_0 is choose arbitrarily to exclude the unknown spikes on density gradient caused by turbulence near the sea surface. In this study, the MLD is estimated by fulfilling density difference larger than 0.15 kg m^{-3} that is $\Delta\rho = \rho(\text{MLD}) - \rho(z_0) > 0.15 \text{ kg m}^{-3}$ where $z_0 = 15 \text{ m}$. The z_0 chosen in the study is to avoid the warm layer in the upper 10 m to 12 m formed on the 13th, which may be associated with sudden wind precipitous fall.

The Brunt-Väisälä frequency (N^2) is often used for discussing the density stratification and express as:



$$N^2 = \frac{-g \partial \rho}{\rho_0 \partial z}$$

N^2 was estimated by temperature and salinity measurements of four floats. High N^2 from 25 m to 50 m was consistent with the change of MLD in the concerning period (Fig. 9). During the MJO active phase from 14th to 17th Dec 2018, the MLD was deepened rapidly from 25 m to 50 m in five consecutive days which was captured by the four floats simultaneously. Strong vertical turbulent mixing might cause the rapid decline of MLD, thereby the upper ocean cooling. According to the negative N^2 ubiquitous above MLD, i.e., the inversion of seawater density, the upper ocean was under the unstable conditions. The major forcing for the instability will be discussed in the next part.

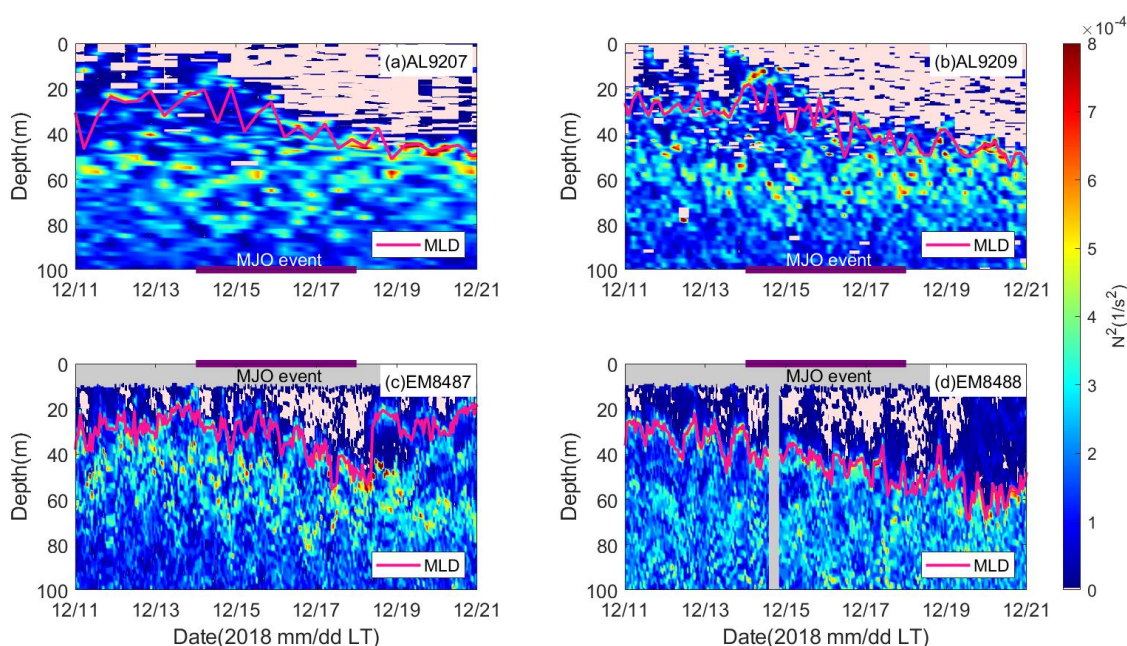


Fig. 9: (a)–(d) Surface MLD (magenta lines) and buoyancy frequency N^2 (shading) derived from two ALAMO floats and two EM-APEX floats measurements AL9207,



AL9209, EM8487, and EM8488, respectively. The negative values of N^2 are expressed with pink dots. The missing data are expressed with gray dots.

4.2 Gradient Richardson number

The study discusses the stability within the stratified shear flow by computing the gradient Richardson number (Ri), which also aims to find where the probable turbulent mixing happened. It is defined as

$$Ri = \frac{N^2}{S^2} = \frac{\frac{-g \partial \rho}{\rho_0 \partial z}}{\left(\frac{\partial U}{\partial z}\right)^2 + \left(\frac{\partial V}{\partial z}\right)^2}$$

where N^2 is buoyancy frequency, g is the gravity acceleration, ρ is the situ density, ρ_0 is the reference density, S is the vertical shear term, U is eastward components, V is eastward component of current, and z is the vertical coordinate. Ri is the proportion of stratified layer and shear flow. If the shear flow supplies sufficient kinetic energy, turbulence can overcome the stratified barrier, and mixing occurs. Miles (1961) and Howard (1961) demonstrated that Ri, of 0.25, is a linear stability threshold. Weak stratified or strong shear within the stratified shear flow can result in $Ri < 0.25$ and generate shear instability. The enhanced shear production term in the TKE budget will favor the growth of turbulence and thereby turbulent mixing. Contrastingly, when $Ri > 0.25$ everywhere in the fluid, flows are stable.

Ri was computed by EM8487 and EM8488 velocity and density measurements (Fig.



10). When the MJO convective arrived, Ri less than 0.25 occurred frequently above the MLD on EM8487 and EM8488. Within the MLD, the horizontal current was accelerated by stronger wind MJO brought, making the shear term in Ri large enough to reach the threshold of 0.25. Namely, due to the stronger current and night time surface cooling, instability occurred above the MLD. The instability might contribute to the density inversion in the ML, and the deepening of MLD should result from the corresponding turbulent mixing.

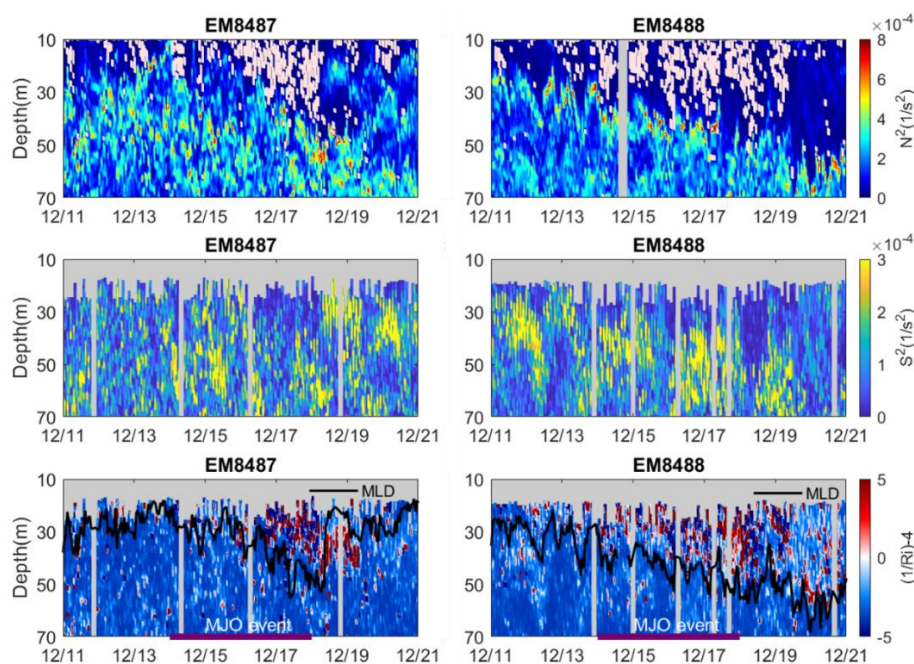


Fig. 10: (a) and (d) are the buoyancy stratification N^2 (shading) derived from EM8487 and EM8488. The negative values of N^2 are expressed with pink dots. (b) and (e) are vertical shear square of EM8487 and EM8488 (c) and (f) are $(1/Ri) - 4$ and surface MLD (black lines) of EM8487 and EM8488. The missing data are expressed with gray dots.



4.3 Thorpe scale method and dissipation rate

Based on the observed N^2 and small Ri at the floats, strong turbulent mixing occurred and related to the passage of MJO's deep convection. Here, we will estimate the turbulent kinetic energy (TKE) dissipation rate to quantify the magnitude of turbulent mixing. Thorpe (1977) assumes the kinetic energy of turbulent eddy transfers to potential energy, resulting in the displacement of a fluid particle. Explaining more, the density measurements profile is reordered to a gravitationally stable profile in which density increase with depth. The fluid particles' vertical distance must be moved adiabatically in this process, and the density displacement is Thorpe displacement. The Thorpe scale is computed by using the root mean square of Thorpe displacement. The turbulent dissipation rate is estimated by Thorpe scale (Fig. 11), using EM8487 and EM8488 density profiles. The estimation of turbulent dissipation rate is approximately between 10^{-8} to 10^{-6} $W\ kg^{-1}$ above the MLD during the MJO active phase. The number is more significant than the estimated value of low wind conditions in the area, which was about 10^{-11} to 10^{-10} $W\ kg^{-1}$ within the thermocline.

When current shear is strong enough or stratification is weak enough, the Ri will decrease to reach the threshold of < 0.25 . It will result in Kelvin-Helmholtz instability. Because of the westerly wind (Section 3), the vertical shear of horizontal current could



be $3 \times 10^{-4} \text{ s}^{-2}$. Despite strong stratification within the thermocline, Ri lowered by the strong vertical shear was typically below 0.25 in the upper ocean. The shear instability associated with the low Ri might enhance turbulence kinetic energy, which would ultimately become potential energy or heat. The momentum from wind stress contributed to current shear that countered the stabilizing effect of density stratification, thereby generating the shear instability. To sum up, the change of MLD during our experiments was forced by the momentum transition from wind to current flow. The entrainment of cold water might then cool the SST.

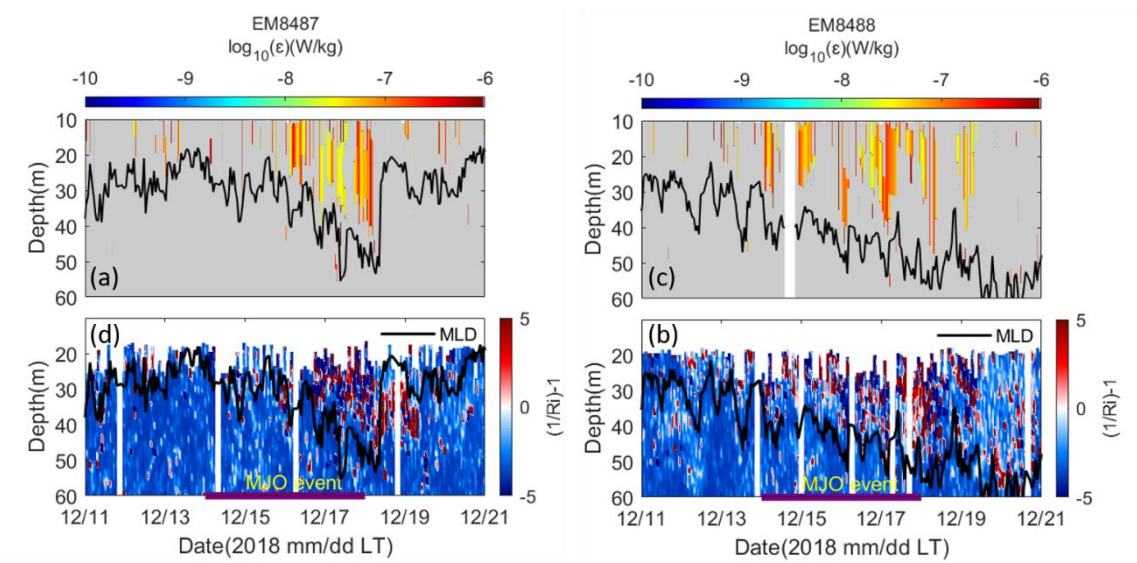


Fig. 11: (a) and (b) are TKE dissipation rate and MLD (black lines) estimated by Thorpe scale method. The value below 10^{-11} are denoted with gray dots. (c) and (d) are $(1/Ri) - 4$ and surface MLD (black lines).

4.4 Summary of mixed layer depth deepening



When the MJO convection event arrived, the wind accelerated the horizontal current to around 0.4 m s^{-1} . The enhanced vertical shear due to the significant current velocity will decrease Ri to less than 0.25 in the ML. In other words, the enhanced vertical shear should be the major factor causing the deepening of ML by inducing the shear instability. Thorpe scale method was used to estimate the turbulent dissipation rate during this turbulent mixing event. The estimated turbulent dissipation rate within the MLD was about 10^{-8} to $10^{-6} \text{ W kg}^{-1}$, more significant than that within the typical thermocline of about 10^{-10} to $10^{-9} \text{ W kg}^{-1}$. Strong turbulent mixing might be the major factor leading to the MLD deepening from 25 m to 50 m via the shear instability in this event.

5 Effect of Turbulent Mixing under MJOs



The rapid deepening of MLD by more than 25 m in five days was observed at two ALAMO floats and two EM-APEX floats. According to the float measurements, the MLD deepening may affect the SST cooling magnitude. Because the SST variation to model forecast is crucial, this study will simulate the MLD deepening caused by wind-induced mixing. Previous studies have demonstrated the critical effect of vertical resolution and mixing parameters on the simulation of turbulent mixing (Large et al. 1994), thereby the variations of SST. These two factors will be discussed in the following. Because EM8488 far away from the buoy may not have the similar wind field as that at buoy, the ocean response at EM8488 will not be discussed.

5.1 Model description

Large et al. (1994) developed the K-profile parameterization (KPP) ocean boundary layer (OBL) parameterizations model to study turbulent mixing within the ocean. The turbulent vertical velocities of unresolved eddies within OBL are expressed as the vertical divergence of the turbulence kinematic fluxes, leading to the time evolution of properties, such as temperature, salinity, and momentum. In KPP, vertical turbulent mixing is parameterized using the gradient Richardson number (Ri_g) and the bulk Richardson number (Ri_b).



Ri_b is expressed in:

$$Ri_b = \frac{(B_r - B(d))d}{(V_r^2 - V^2(d)) + V_t(d)}$$

B_r and V_r are mean buoyancy and velocity, d is depth and V_t include other effects such as convection or non-local entrainment. The depth of OBL is at where Ri_b equals to critical value Ri_c . Due to the strong eddy diffusivity, the vertical structure in OBL is almost homogeneous

We use KPP in one-dimensional Regional Oceanic Modeling System (ROMS; Shchepetkin and McWilliams 2005) to simulate the evolution of the upper ocean structure. Float measurements in the upper 200 m are averaged from 12th Dec 1:00 p.m. to 13th Dec 6:00 a.m. as the initial conditions. Below 200 m, the missing measurements of temperature, and salinity and horizontal current are compensated with Hycom data. AL9207 and AL9209 do not have the current data so the initial conditions are completely filled with Hycom data. The forcing term utilize buoy measurements, including wind, air temperature, humidity, air pressure, shortwave, and longwave radiation. The run starts on the 13th Dec when was one day before the arrival of MJO. The temporal resolution is 600 s. The default setting of mixing parameters critical gradient Richardson number equal 0.7 and critical bulk Richardson number equal 0.3. The vertical resolution is about 1 m from 110 m depth to the ocean surface.

5.2 Simulating mixed layer depth deepening



The simulation of surface MLD is compared to the observation (Fig. 12). To avoid the impact of eddy which is located at the south of floats after 15th Dec, the comparison focuses on 13th to 14th when the westerly wind rose up. The model does not predict the MLD deepening during the MJO active phase as that observed by the three floats. On AL9207 and EM8487, the result of MLD deepening rate is underestimated with a difference of 5 m to the observations. Because the change of MLD is affected by the turbulence simulating, some previous studies suggested some factors, including resolution and KPP parameter (Critical Bulk Ri, Critical Gradient Ri), affect MLD performance in KPP. Therefore, the sensitive test of the resolution, KPP parameter will be described in the following section.

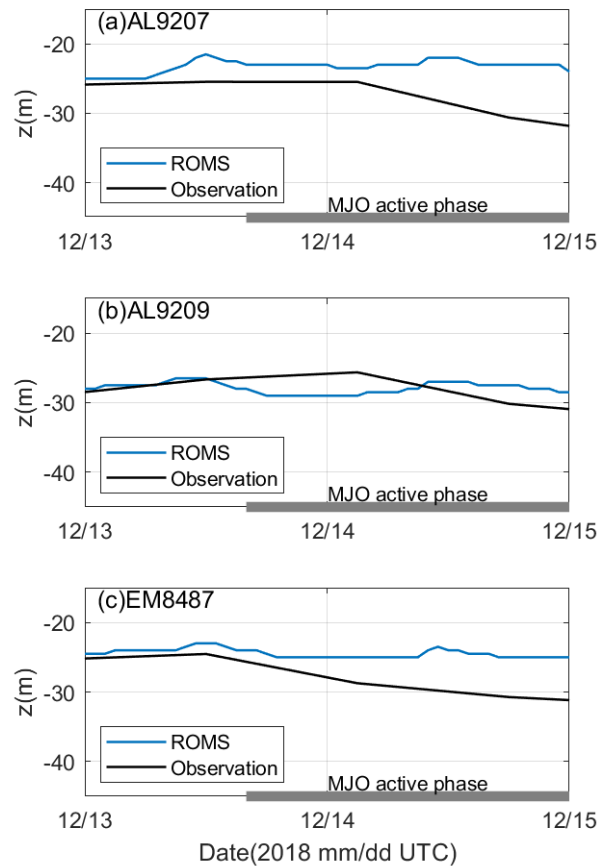
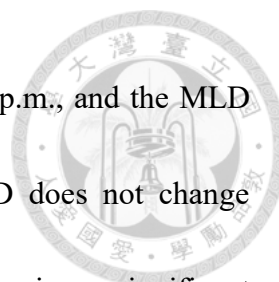


Fig. 12: (a)–(c) Simulations of MLD deepening at the different initial conditions of three floats in KPP (blue line), with the comparison to the float observation (black line).

5.3 Effects on vertical resolution in the upper ocean

Vertical resolution is required to capture a small scale, such as vertical mixing features in the equatorial ocean (Jia et al., 2021). Woolnough et al. (2007) and Bernie et al. (2008) have proposed that increasing vertical resolution to around 1 m is critical for simulating SST variations during the MJOs. In this study, the vertical resolution of 1 m, 2 m, and 4 m in upper 110 m are used in MLD deepening simulation (Fig. 13). In the



model, the MLD of AL9207 shallows about 5 m on Dec 13th at 12 p.m., and the MLD maintains about the same depth in the following days. The MLD does not change significantly in the three floats during the MJO. Furthermore, there is no significant difference between high resolution and coarse resolution on MLD. The results demonstrate that the vertical resolution apparently does not act on MLD performance in this case.

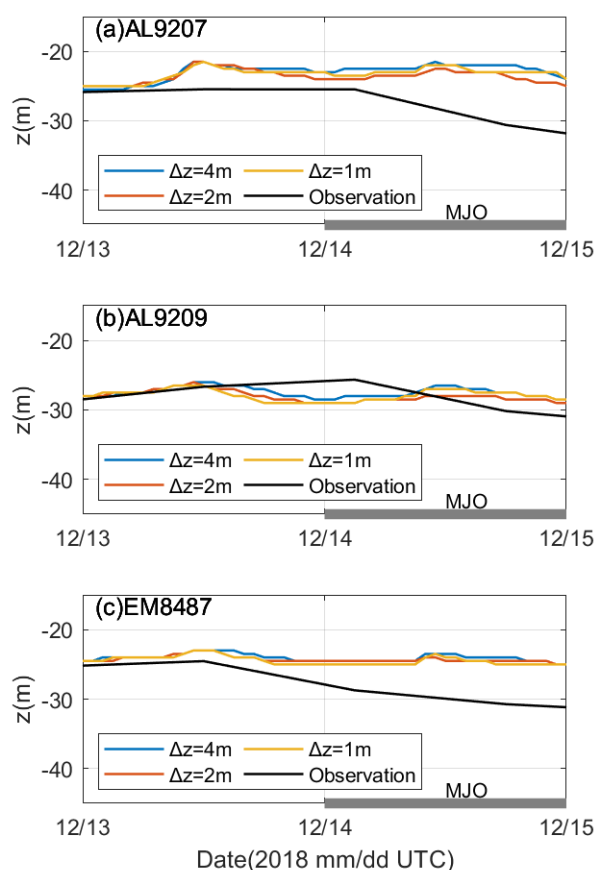


Fig. 13: Different vertical resolutions on simulations of MLD (a)–(c) at AL9207, AL9209, and EM8487 (blue: 4 m; orange: 2 m; yellow: 1 m), with the comparison to the float observation (black line).

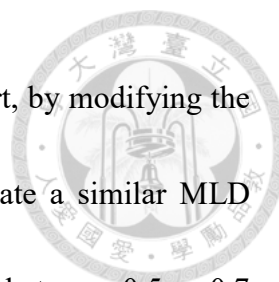


5.4 Parameters in the KPP mixing scheme

In the KPP, the parameters Ri_0 and Ri_c directly affect the vertical diffusivity $K\rho$ within and below the OBL, and these may result in difference of turbulence simulating. The effects of these two parameters are studied.

Ri_0 is increased from 0.7 to 1, resulting in stronger turbulence induced by shear at the base of OBL (Fig. 14). However, the KPP still fails to simulate the MLD deepening depth. The values of Ri_0 are tested to make the simulated MLD similar with the observation depth. The model results are not similar to the observation unless Ri_0 of 5 was used. Although strengthening and extending the turbulent mixing at the base of OBL can obtain a similar result to observation, the value is too large and not real in general ocean conditions. Moreover, when Ri_0 decreases from 0.7 to 0.3, more challenged to induce shear instability. The MLD is not significantly variable, either.

On the other hand, increasing the Ri_c from 0.3 to 0.7 forces the KPP to simulate a thicker OBL (Fig. 15). That is, increasing the Ri_c value may enhance wind effect on destratifying all stratification to a deeper layer. When wind forcing became stronger at about 13th 12 pm UTC, different Ri_c used in the model will cause the variations of simulated MLD. When Ri_c equals 0.5, MLD is similar to the observation on AL9209. On AL9207 and EM8487, the results by tuning Ri_c to 0.7 can also make simulation of MLD



close to the observation MLD when the wind field increases. In short, by modifying the parameters Ri_c can reach a deeper KPP boundary layer and simulate a similar MLD variation of observation when the wind started. However, the value between 0.5 or 0.7 does not correspond to typical ocean conditions (Geernaert 1990). Because the observed change of MLD is due to the wind-driven shear instability, the momentum flux during the model simulation can also significantly affect the ocean current. Therefore, the next section will discuss the sensitive test of momentum flux.

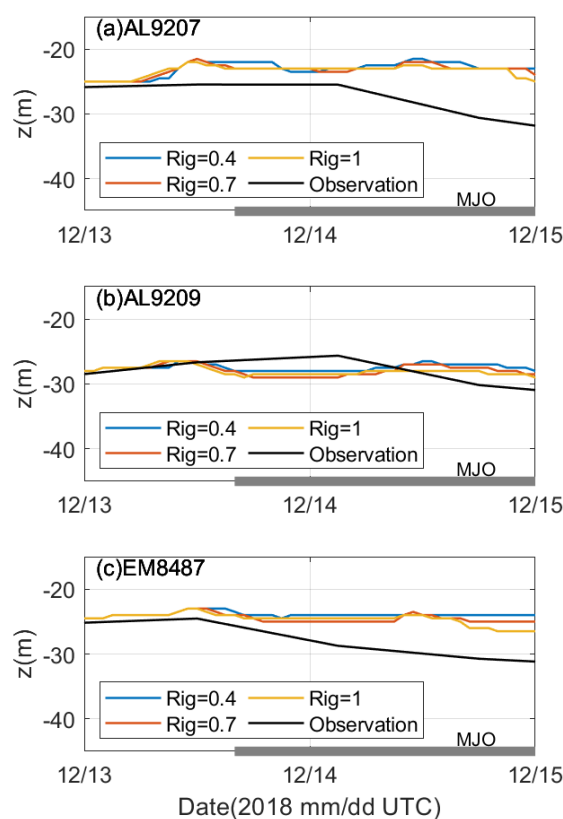


Fig. 14: Different gradient Richardson number on simulations of MLD (a)–(c) at AL9207, AL9209 and EM8487 (blue: $Ri_0 = 0.4$; orange: $Ri_0 = 0.7$; yellow: $Ri_0 = 1$), with the comparison to the float observation (black line).

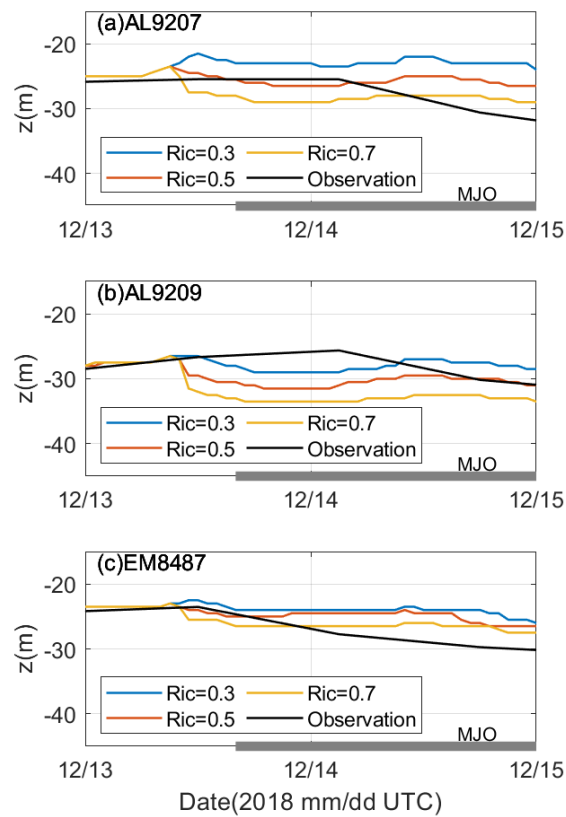



Fig. 15: Different bulk Richardson number on simulations of MLD (a)–(c) at AL9207, AL9209 and EM8487 (blue: $Ri_c = 0.3$; orange: $Ri_c = 0.5$; yellow: $Ri_c = 0.7$), with the comparison to the float observation (black line).

5.5 Summary of MLD simulation by using KPP

We use KPP in one-dimensional ROMS to simulate the MLD deepen under the buoy wind measurement. With the default parameters set in KPP, the MLD deepening depth do not simulate well on MLD deepening. In the model, MLD does not change significantly in the first two MJO days. Because the vertical resolution, critical gradient Ri , and critical



bulk Ri can affect MLD performance in KPP, the sensitive tests are performed to explore these factors' effects on MLD simulations. The vertical resolution and critical gradient Ri do not affect apparently on the MLD. Although tuning critical to 0.7 bulk Ri can obtain similar MLD, this high value of 0.7 does not correspond to typical ocean conditions. Therefore, adjusting the parameters in the KPP may not be appropriate for simulating the observed MLD deepening during the MJOs. Other factors will be discussed in the section.



6 Momentum and Buoyancy Response during MJOs

According to the adjustment on the parameters in KPP, the critical bulk Richardson number can affect the MLD simulation significantly. However, when we tune Ri_c to match the MLD of observation, the value must be larger than typical ocean conditions (~ 0.3). Because the MLD deepening is caused by shear instability, the simulated horizontal current velocity will affect the MLD deepening significantly.

Here, we compare the model results with the observed current velocity at EM8487. The observed current in the upper 20 m is larger around 0.05 m s^{-1} than ROMS result (Fig. 16). In other words, the simulation of momentum flux may be underestimated, which will lead to the different current velocity on simulation. Below, we will discuss the effect of the drag coefficient C_d , which will affect the computation of surface wind stress. Furthermore, because buoyancy flux can affect the MLD deepening, the effect of heat flux will be discussing in this section, too.

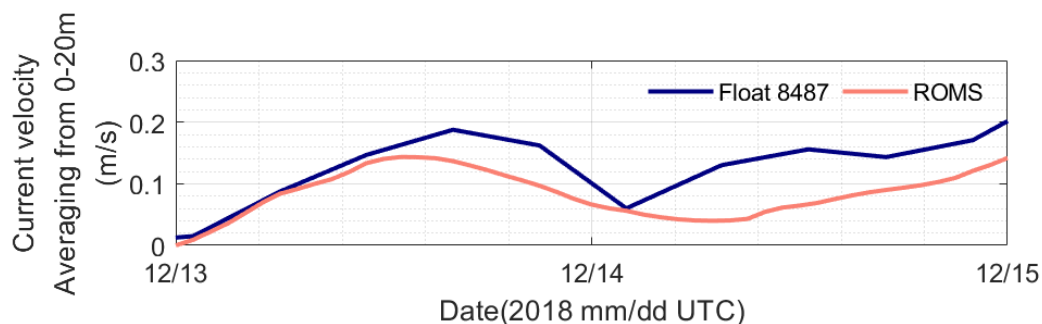


Fig. 16: Current velocity averaged from 0 m to 20 m depth of EM8487 (blue line) and ROMS (orange line).



6.1 Wind drag coefficient

Surface wind stress (τ), generated by wind momentum, forces ocean current. It is commonly parameterized with a drag coefficient (C_d) and expressed as $\tau = C_d \rho_{\text{air}} U_{10} |U_{10}|$ where ρ_{air} is the air density, and U_{10} is wind velocity at 10 m above the sea surface. In ROMS, COARE 3.0 algorithm (Fairall et al. 2003) is used to estimate wind stress. However, momentum flux in the model is probably underestimated, resulting in current and shear failing to simulate well (Fig .16). Thus, wind stress estimated from COARE 3.0 in ROMS is multiplied 1.2, 1.5, and 1.8 times and then simulated the MLD deepening again. That is, the transferred wind momentum from the atmosphere into the ocean is artificially increased. When the wind stress was increased by larger C_d , MLD deepening simulated well on MLD depth on the three floats (AL9207, AL9209, EM8487). Therefore, whether the wind stress estimated by COARE 3.0 is underestimated that leads to the underestimated deepening of MLD needs to be studied. In the next part, the wind-induced current will be extracted from float measurement to quantify the observed momentum flux during the field experiment.

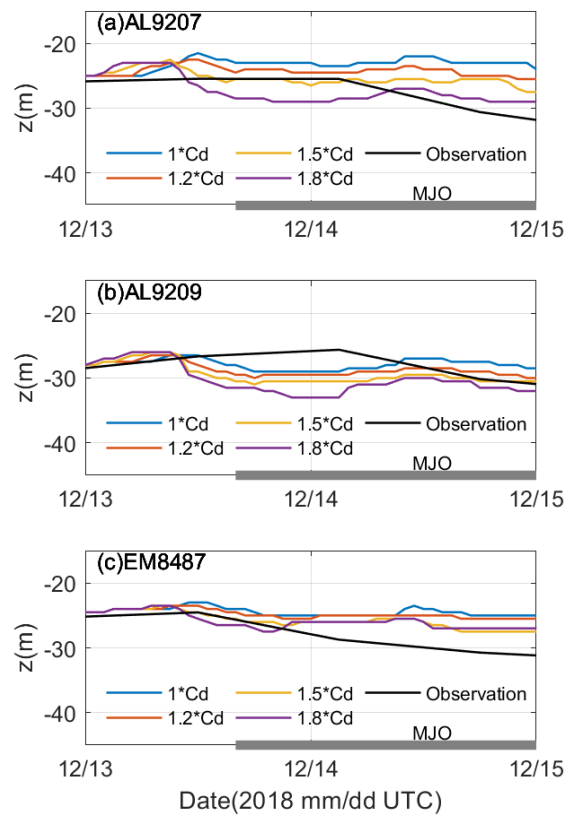


Fig. 17: Different magnitude of wind stress on simulations of MLD (a)–(c) at AL9207, AL9209 and EM8487, (blue: wind stress estimated from COARE 3.0; orange: 1.2 times; yellow: 1.5 times; purple: 1.8 times of wind stress), with the float observation (black line).

6.2 Wind-induce current

For the purpose of computing the current momentum obtained from the surface wind stress, non-wind-driven currents must be excluded from the raw measurements. Fast Fourier Transform (FFT) is applied to the current velocity measurement, in order to find the dominant current components from 1st to 31th Dec in the upper 50 m. Two peak signals are found, including a 43.5 h period and a 12.5 h period which is regarded as inertial



motion and semi-diurnal M2 tide, respectively (Fig. 18). As a result, the primary constituent of float measurement current is written in:

$$V = V_{\text{inertial}} + V_{\text{semi-diurnal}} + V_{\text{background}}$$

With the bandpass filter, the magnitude of $V_{\text{semi-diurnal}}$ is extracted (Fig.19). The semi-diurnal tides are extracted with a period between 11 h and 14 h, and the magnitude is up to 0.1 m s^{-1} . Previous model studies and observations in the region also found the same stronger semi-diurnal tides (Holloway et al. 2001; Rayson et al. 2011). The inertial motions are extracted with a period between 41 h and 46 h. The magnitude is generally less than 0.05 m s^{-1} .

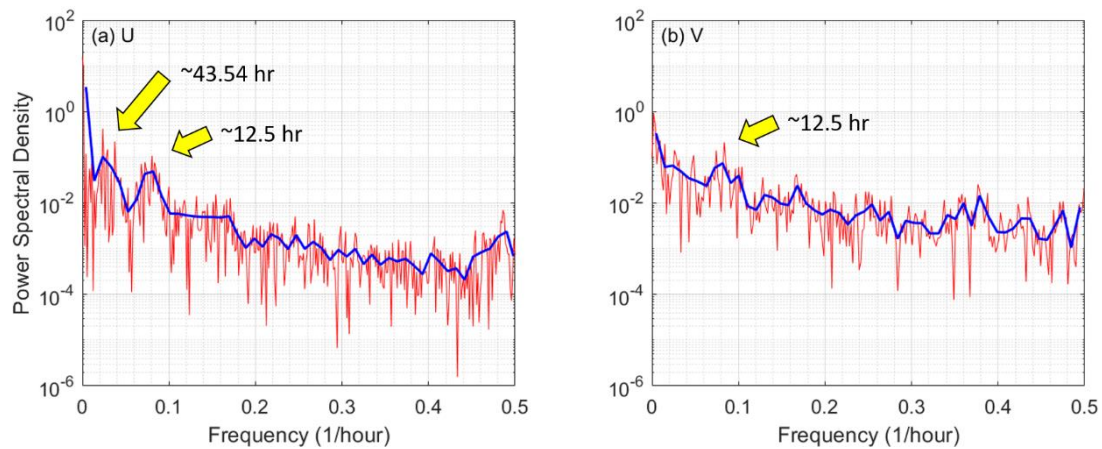


Fig. 18: Power spectrum density of (a) east-west current and (b) north-south current.

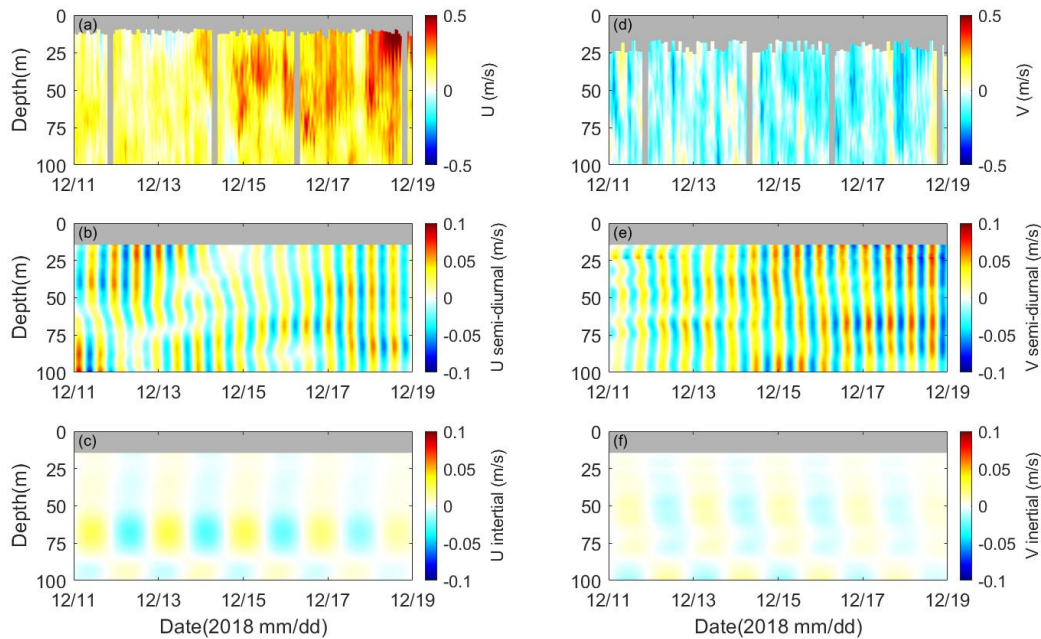
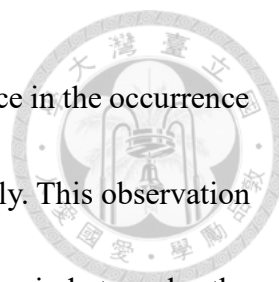


Fig. 19: East-west components of (a) current velocity, (b) semi-diurnal-tide, and (c) inertial current; north-south components of (d) current velocity (e) semi-diurnal-tide, and (f) inertial current. The missing data are expressed with gray dots.

The inertial motions in the upper ocean are regarded as generated by the local wind. The wind-induced current is estimated using the float measurement, after excluding the semi-diurnal tide and the background current that averages the current velocity before the MJO. The result is compared to the model result with no current as the initial condition (Fig. 20). A 43.5 h period current is found in both observation and model results in the upper ocean. By lag-correlation, 14 h lags on east-west and 12 h lag north-south components (not shown) are discovered between the model and observation. The spatial



variation of wind between the floats and buoy may cause the difference in the occurrence time of MLD deepening, so we shift the phase of model results slightly. This observation of wind-induced current and model results will be used to compute wind stress by the linear momentum budget method.

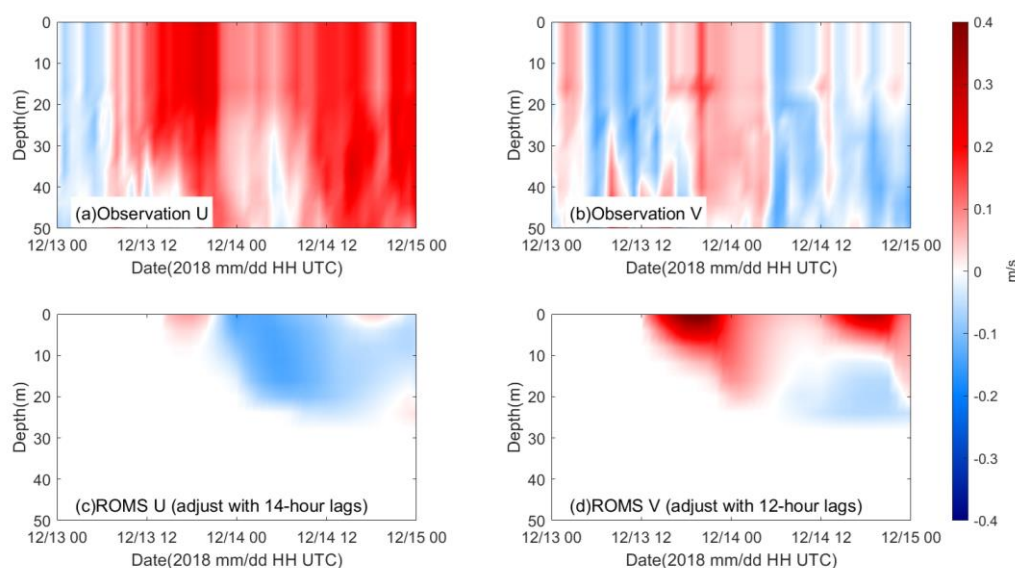


Fig. 20: (a) East-west and (b) north-south component of EM8487 measurement excluding semi-diurnal tides and background current (c) East-west and (d) north-south component of ROMS results which have been adjusted with time lags.

6.3 Linear momentum budget method and wind stress

6.3.1 Linear momentum budget method

The surface wind stress is estimated following Sanford et al. (2011) and Hsu et al. (2017). Using the EM8487 wind-induced current velocity profiles computes the depth-



integrated on linear momentum balance equation that is:

$$\frac{\partial V}{\partial t} + V \cdot \nabla V + f\hat{k} \times V = -\frac{1}{\rho_0} \nabla p + \frac{1}{\rho_0} \frac{\partial \tau}{\partial z} - \frac{\rho}{\rho_0} g\hat{k}$$

where V is the ocean current velocity, f is Coriolis frequency (around rad s^{-1} at 16°S), ρ is the situ density, ρ_0 is Boussinesq density, and τ is the stress vector. The depth-integrated

horizontal momentum equation from sea surface to depth $-z$ is:

$$\int_{-z}^0 \left(\frac{\partial v_h}{\partial t} + v_h \nabla_h \cdot v_h + v_h \cdot \nabla_h v_h + f\hat{k} \times v_h + \frac{1}{\rho_0} \nabla_h p \right) dz = \frac{(\tau_0 - \tau_{-z})}{\rho_0} + w_{-z} V_{-z}$$

where the horizontal current ($V_h = u\hat{i} + v\hat{j}$) and gradient operator ($\nabla_h = \partial/\partial x \hat{i} + \partial/\partial y \hat{j}$),

τ_0 is the surface wind stress, τ_{-z} is turbulence stress. V_{-z} is horizontal velocity. Here assuming τ_{-z} and $w_{-z} V_{-z}$ are zero. During the forcing stage of wind (Sanford et al. 2011),

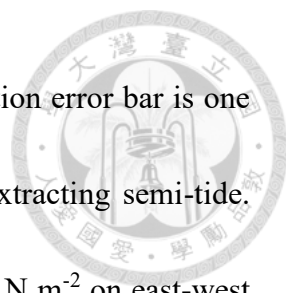
nonlinear and pressure gradient terms may be negligible. Due to this assumption for neglecting the nonlinear and pressure gradient terms, there will be an error in estimated

($\Delta\tau$). Thus, surface wind stress (τ_0) derived from depth-integrated linear momentum equation:

$$\tau_0 = \tau + \Delta\tau = \rho_0 \int_{-z}^0 \left(\frac{\partial v_h}{\partial t} + f\hat{k} \times v_h \right) dz$$

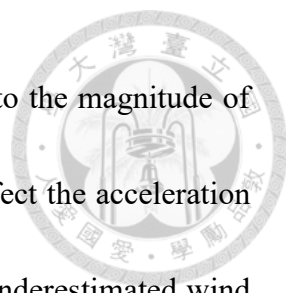
6.3.2 Wind stress

According to depth-integrated linear momentum equation, the time rate change on horizontal momentum and Coriolis force is estimated by float's wind-induced current and



model results via integrating to 100 m depth (Fig. 21). The observation error bar is one deviation with different time-averaging background currents and extracting semi-tide. Coriolis force terms of observation are adjusted with the offset 0.35 N m^{-2} on east-west momentum and 0.15 N m^{-2} on north-south momentum that is contributed by the eddy of which current velocity is about 0.2 m s^{-1} and 0.08 m s^{-1} , respectively. We focus on the wind stress variation on the first day of MJO to avoid unknown momentum transfer.

During the wind forcing period, the time rate change of velocity in the model results is less than the observation. The value of observation is up to 0.3 N m^{-2} and -0.25 N m^{-2} on northward and eastward components, respectively. Contrasting to the observation, the model result is about 0.1 N m^{-2} on the original wind stress. The difference comes to 0.2 N m^{-2} between observations. The result shows that the wind stress does not efficiently input to the ocean in the model. Because the wind stress is the function of C_d and wind speed, C_d may be underestimated, or the wind speed on the float position is larger than the buoy. When C_d multiple to 1.8 times, the value is similar to observation. The result demonstrates that increasing the wind stress can obtain a similar momentum flux to the observation. On the other hand, the Coriolis force on the model is also less than the observations. The meridional and zonal components are both about 0 N m^{-2} at Dec 13th 12 p.m. During the MJO, Coriolis force changes to 0.175 N m^{-2} in the first inertial current period on both northward and eastward components. By contrast, the model results are



about 0.1 Nm^{-2} . The multiple of the C_d to 1.5 times can be similar to the magnitude of observation. Namely, the wind stress difference can significantly affect the acceleration rate of horizontal current. MLD simulation may be affected by the underestimated wind stress.

Note that there are two aspects of underestimated wind stress. Firstly, the drag coefficient used in the model simulations is from the COARE 3.0 algorithm. The underestimated momentum flux due to an inappropriate drag coefficient may affect the MLD and SST simulation during the MJO active phase. However, the 1.8 times C_d may be larger too large (Fig. 22). Secondly, the wind stress is estimated by 10-m height wind magnitude. The wind stress as a function of wind speed square. When the wind speed increases by 1.35 times, the wind stress will increase by about 1.8 times simultaneously. Due to the different locations of the buoy and the three floats (AL9407, AL9409, EM8487), the wind above the sea surface of the float may be an anomaly to the buoy. The possible wind speed difference leads to an underestimate of the wind stress. To sum up, compared to the observation, the wind stress was underestimated in the model, resulting in the failure of MLD simulation. This may cause by the inappropriate drag coefficient, or the wind forcing term cannot represent those above the float. In the next section, because the buoyancy flux affects the deepening of MLD, the buoyancy will be considered in the simulation.

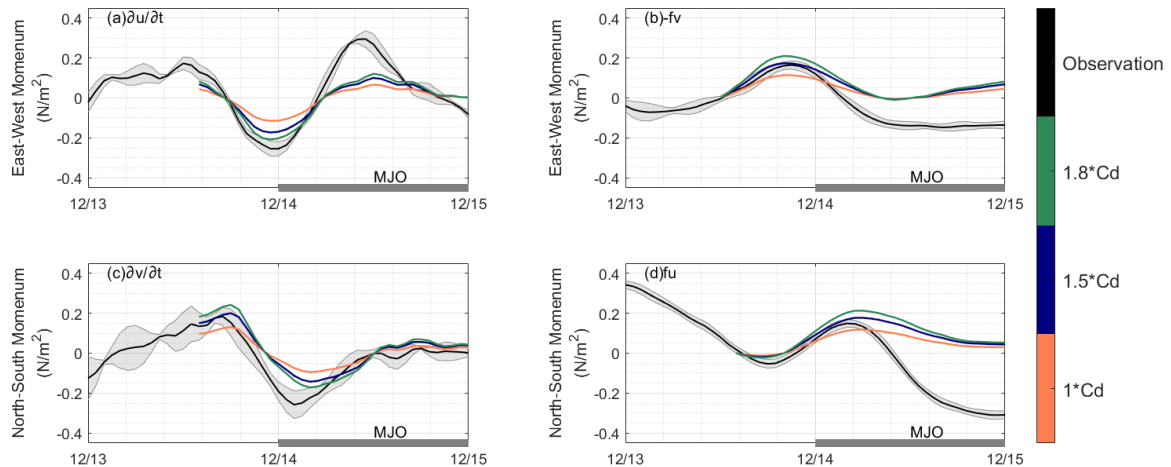


Fig. 21. Depth-integrated comparisons of float observations (black line with one standard deviation error bars) and KPP simulations (orange: COARE 3.0 estimated; blue: 1.5 times; green: 1.8 times of wind stress) during the MJO. (a) and (c) is the time rate change momentum of U and V components, respectively. (b) and (d) is Coriolis force terms of U and V components, respectively.

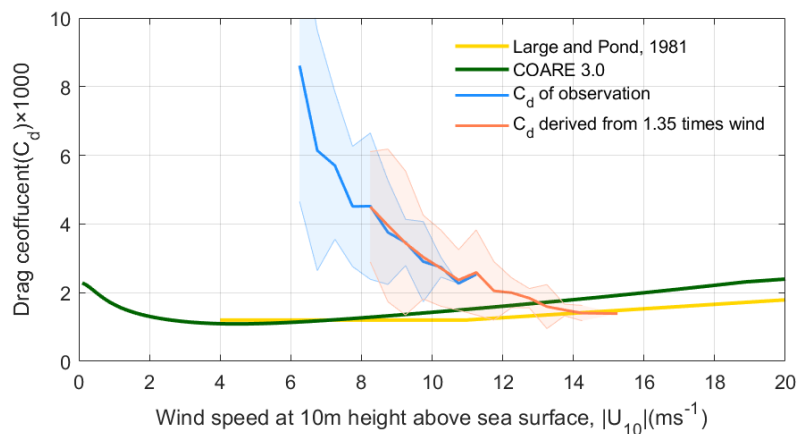


Fig. 22: The drag coefficient C_d as a function of wind speed at 10 m above the sea (yellow: Large and Pond, 1981; green: COARE 3.0 estimated; blue: derived from observation; orange: derived from 1.35 times of wind with one standard deviation error bars)

6.4 Buoyancy flux effect



During the nighttime, ocean heat transfer to the atmosphere leads to sea surface cooling. Due to the cooling, the sea surface water density increases and sink. The process results in turbulent convection, and MLD may deepen during this. Thus, the value of the heat flux, which considers the sea surface cooling magnitude, may affect the MLD. The latent and sensible heat flux is associated with the air temperature difference and the wind speed. To find the possible effect of the temperature and wind speed anomaly, the $\pm 50 \text{ W m}^{-2}$ of the estimated heat flux as these anomalies effect and be simulated again. The result demonstrated that increasing 50 W m^{-2} of heat flux allows the MLD to deeper, around 2 m. Contrastingly, the MLD of decreasing 50 W m^{-2} is 2 m shallower than the original heat flux input. This means the heat flux affects the MLD simulation. As a result, the buoyancy effects are required to consider in the simulation. However, the possibility effect of buoyancy flux, around $\pm 2 \text{ m}$, is not much more significant than the wind stress effect (Fig. 22). The model results are not similar to the observation unless more than 400 W m^{-2} is used (not shown). The value is too large and irrelevant in this area (Marshall and Hendon, 2014). To conclude, the model study finds that critical Richardson numbers, wind stress, and heat flux may result in the MLD deepening simulation accuracy during MJO. Among them, appropriate wind stress input is much more crucial in simulating

MLD during the MJO. Future forecasts may further explore the reliable surface wind stress or drag coefficient for simulating the ocean response to MJOs.

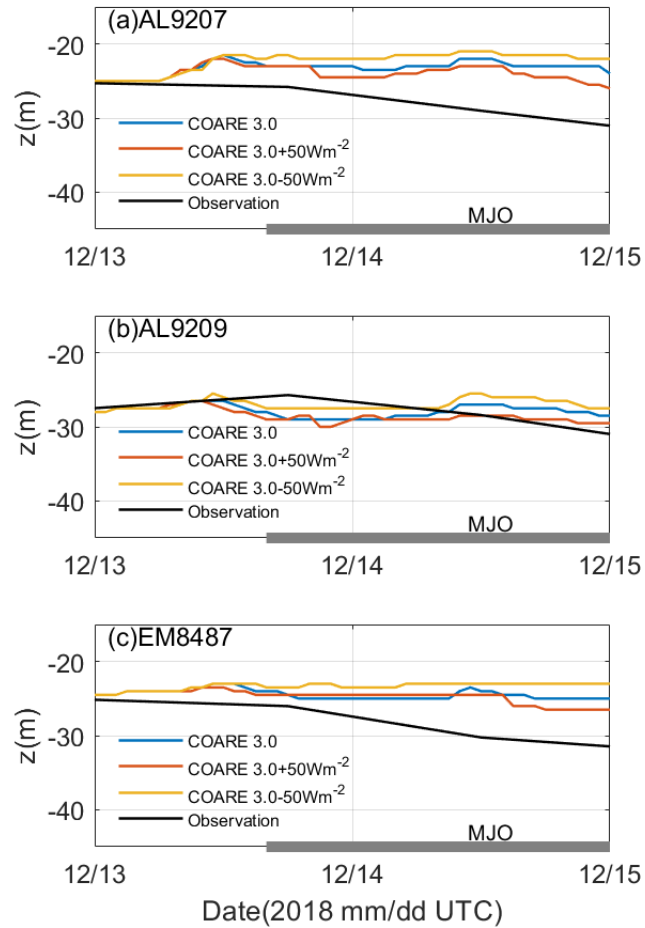
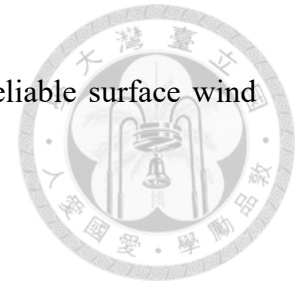


Fig. 23: The heat flux input in MLD simulation of COARE 3.0 estimated (blue line); estimated value + 50 W m⁻² (orange line); estimated value - 50 W m⁻² (yellow line) compare to the float observation (black line) at (a)–(c) at AL9207, AL9209 and EM8487.

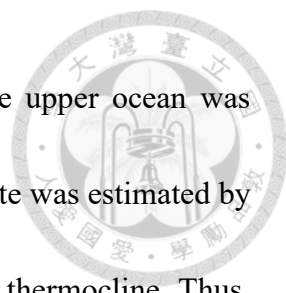
7 Conclusion and discussion



Six ALAMO floats, two EM-APEX floats, and a buoy were deployed in northwest Australia on 22nd Nov 2018 (Feng et al. 2020). In the middle of December 2018, two ALAMO floats, and two EM-APEX floats remained and recorded the ocean temperature, salinity, and horizontal velocity during one MJO event when was from 14th to 18th Dec. These data sets aided us in exploring the upper ocean response to the MJO and heat flux variation to the MJO's deep convection.

MJOs are typically associated with a westerly wind. During the MJO, the wind speed rose to around 10 m s⁻¹. In the upper ocean, the current velocity forced by the wind increased up to 0.4 m s⁻¹ above 40 m. At the same time, an upper ocean and SST cooling event were observed since 14th Dec. The temperature in the upper 40 m dropped about 1.1 °C in one day. The cold water below the MLD should entrain into the upper ocean and cool the SST near the sea surface. Due to the drop in SST, the difference between air temperature and SST changed. In addition, the wind speed also favored evaporation. As a result, air-sea heat flux was modified to rise from 100 Wm⁻² to 400 Wm⁻².

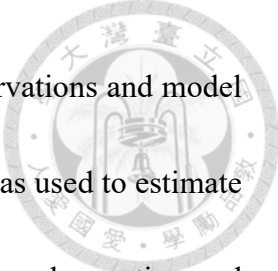
The MLD was deepened from 25 m to 50 m during this MJO period. By using the float measurements, the buoyancy frequency was computed and was frequently less than zero within the MLD. Additionally, the vertical shear was up to 3 3×10⁴ N m⁻². These



allowed the Richardson number to be less than 0.25, implying the upper ocean was unstable. Using the Thorpe scale method, the turbulent dissipation rate was estimated by 10^{-8} to 10^{-6} W kg⁻¹. These were larger than those within the typical thermocline. Thus, strong turbulent mixing happened via shear instability during the MJO, resulting in MLD deepening. This process allowed the cold water below the MLD to be entrained into the upper ocean, resulting in SST cooling.

We used KPP in one-dimensional ROMS to simulate the MLD deepen under the buoy wind measurement. In the model, MLD did not consist of observation MLD and did not change significantly in the first two MJO days. Sensitive tests on the effect of vertical resolution and mixing parameters were used to find the critical factor in simulating turbulent mixing under MJO. By tuning the turbulence simulation parameter, increasing the critical bulk Richardson number significantly affected the MLD simulation in that higher critical bulk Richardson number was able to reach a deeper KPP boundary layer.

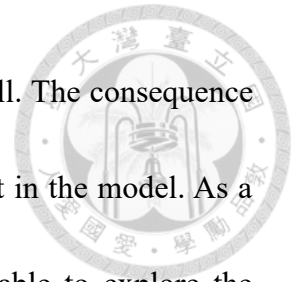
Comparing the current velocity between the observations and model, the mean current velocity in the upper 20 m was 0.2 m s⁻¹ and 0.1 m s⁻¹, respectively. The difference in current acceleration rate will result in different wind stress fluxes. The drag coefficient is adjusted manually to perform the sensitive test, so different magnitudes of surface wind stress will be used for forcing the ocean current. According to the model simulations, the simulated results of MLD do not agree well with the observations unless 1.8 times of

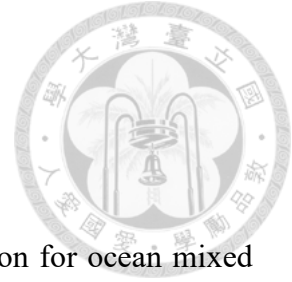


wind drag coefficient is used. The momentum flux between the observations and model results might be different. As a result, the linear momentum budget was used to estimate wind stress. The results demonstrated that the difference between the observation and model was about 0.2 N m^{-2} and 0.075 N m^{-2} in time rate change on velocity and Coriolis force, respectively. Thus, the wind stress estimated by COARE 3.0 may be underestimated in ROMS, resulting in the MLD being inconsistent with observation. Even considering the buoyancy effect by tuning the heat flux with $\pm 50 \text{ W m}^{-2}$ as the uncertain wind speed and temperature variation, the effect is just about 2 m discrepancies. Despite the fact that buoyancy allows MLD to get deepen. However, the wind stress effect is more significant than buoyancy in MLD simulation under the MJO wind field. Therefore, COARE 3.0 still underestimated wind stress on MLD simulation under MJO when considering the buoyancy effect on turbulence simulation.

In summary, the high wind speeds during the active phase of MJOs trigger the ocean current and thereby larger vertical shear for the growth of turbulence. The vertical velocity shear should destabilize the upper ocean during the MJO. The turbulence mixing at the base of MLD allows the cold water entrains to upper and cool down the SST. Due to the SST variation, heat flux is modified and may influence the MJO convection developments. In the model, wind stress estimation is the critical factor in MLD simulation. The wind stress scheme from the COARE 3.0 algorithm in ROMS should be underestimated during

the MJO, which will result in the failure of the MLD simulation well. The consequence of MLD failing to simulate may affect MJO simulation and forecast in the model. As a result, field measurements on ocean current and wind speed are able to explore the momentum flux between air-sea during MJOs. The correct wind stress estimation may also improve the MJO forecast by being used in the global coupled model in the future.





Reference

A.B. Kara, P.A. Rochford, H. Hurlburt, (2000). An optimal definition for ocean mixed layer depth. *J. Geophys. Res.*, 105 (2000), pp. 16803-16821.

Bernie, D. J., E. Guilyardi, G. Madec, J. M. Slingo, S. J. Woolnough and J. Cole, (2008). Impact of resolving the diurnal cycle in an ocean–atmosphere GCM. Part 2: A diurnally coupled CGCM. *Climate Dynamics*, 31, 909-925, doi: 10.1007/s00382-008-0429-z.

Chen, D., L.M. Rothstein, and A.J. Busalacchi, (1994). A hybrid vertical mixing scheme and its application to tropical ocean models. *J. Phys.Oceanogr.*,24, 2156–2179.

Cole, R., J. Kinder, C. L. Ning, W. Yu, and Y. Chao, (2011). “Bai-Long”: A TAO-hybrid on RAMA. OCEANS’11 MTS/IEEE KONA, Waikoloa, HI, IEEE, <https://doi.org/10.23919/OCEANS.2011.6106952>

DeMott, C. A., Klingaman, N. P. & Woolnough, S. J. (2015). Atmosphere–ocean coupled processes in the Madden-Julian Oscillation. *Rev. Geophys.* 53, 1099–1154.

Emanuel, K. A., 1995: Sensitivity of tropical cyclones to surface exchange coefficients and a revised steady-state model incorporating eye dynamics. *J. Atmos. Sci.*, 52, 3969–3976, doi:10.1175/1520-0469(1995)052, 3969: SOTCTS.2.0.CO;2.

Fairall, C. W., E. F., Bradley, D. P., Rogers, J. B., Edson, and G. S., Young, 1996a. Bulk parameterization of air-sea fluxes for Tropical Ocean-Global Atmosphere Coupled Ocean Atmosphere Response Experiment, *J. Geophys. Res.*, 101, 3747– 3764, doi:10.1029/95JC03205.

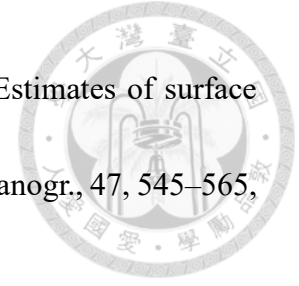
Fairall, C.W., E. F. Bradley, J. E. Hare, A. A. Grachev, and J. B. Edson, 2003. Bulk Parameterization of Air-Sea Fluxes: Updates and Verification for the COARE Algorithm. *J. Climate*, 16, pp 571-591.

Feng, M., Y., Duan, S., Wijffels, J.-Y., Hsu, C., Li, H., Wang, Y., Yang, H., Shen, J., Liu, C., Ning, and W., Yu, 2020. Tracking air-sea exchange and upper ocean variability in the Southeast Indian Ocean during the onset of the 2018-19 Australian summer monsoon. *Bulletin of the American Meteorological Society*.
<https://doi.org/10.1175/BAMS-D-19-6540278.1>.

Friedrich A. Schott, Shang-Ping Xie, Julian P. McCreary Jr (2009). Indian Ocean circulation and climate variability. *Rev. Geophys.*, 47 (1), p. G1002.

Geernaert, G. L., 1990: Bulk parameterizations for the wind stress and heat fluxes. *Surface Waves and Fluxes*, G. L. Geernaert and W. J. Plant, Eds., Vol. 1, Kluwer Academic, 336 pp.

Howard, L. (1961). Note on a paper of John W. Miles. *Journal of Fluid Mechanics*, 10(4), 509-512. doi:10.1017/S0022112061000317.



Hsu, J.-Y., R.-C. Lien, E. A. D'Asaro, and T. B. Sanford, (2017). Estimates of surface wind stress and drag coefficients in Typhoon Megi. *J. Phys. Oceanogr.*, 47, 545–565, <https://doi.org/10.1175/JPO-D-16-0069.1>.

Je-Yuan Hsu, Ming Feng and Susan Wijffels (2022). Rapid restratification of the ocean surface boundary layer during the suppressed phase of the MJO in austral spring. *Environ. Res. Lett.* 17 024031.

Large, W. G., J. C. McWilliams, and S. C. Doney, (1994). Oceanic vertical mixing: A review and a model with a nonlocal boundary layer parameterization, *Reviews of Geophysics*, 32, 363- 403.

Liu, L. L., Li, Y. L., & Wang, F. (2021). MJO-induced intraseasonal mixed layer depth variability in the equatorial Indian Ocean and impacts on subsurface water obduction. *Journal of Physical Oceanography*, 51, 1247– 1263. <https://doi.org/10.1175/JPO-D-20-0179.1>.

Lorbacher, K., Dommenges, D., Niiler, P. P., & Köhl, A. (2006). Ocean mixed layer depth: A subsurface proxy of ocean-atmosphere variability. *Journal of Geophysical Research*, 111(C7). <https://doi.org/10.1029/2003JC002157>.

Lukas, R., and E. Lindstrom, 1991. The mixed layer of the western equatorial Pacific Ocean, *J. Geophys. Res.*, 96(S01), 3343– 3357, doi:10.1029/90JC01951.

Madden, R. A., & Julian, P. R. (1972). Description of global-scale circulation cells in the



tropics with a 40–50 day period. *Journal of the Atmospheric Sciences*, 29(6), 1109– 1123. [https://doi.org/10.1175/15200469\(1972\)029<1109:dogscc>2.0.co;2](https://doi.org/10.1175/15200469(1972)029<1109:dogscc>2.0.co;2).

Marshall, A. G., and H. H. Hendon, (2014). Impacts of the MJO in the Indian Ocean and on the western Australian coast. *Climate Dyn.*, 42, 579–595, <https://doi.org/10.1007/s00382-012-1643-2>.

Marshall, A.G., Hendon, H.H. Impacts of the MJO in the Indian Ocean and on the Western Australian coast. *Clim Dyn* 42, 579–595 (2014). <https://doi.org/10.1007/s00382-012-1643-2>

Miles, J. W. 1961 On the stability of heterogeneous shear flows. *J. Fluid Mech.* 10, 496.

Moum, J. N., S. P. de Szoeke, W. D. Smyth, J. B. Edson, H. L. DeWitt, A. J. Moulin, E. J. Thompson, C.J. Zappa, S. A. Rutledge, R. H. Johnson, and C. W. Fairall, (2014). Air–Sea Interactions from Westerly Wind Bursts During the November 2011 MJO in the Indian Ocean. *Bull. Amer. Meteor. Soc.*, 95, 1185–1199, <https://doi.org/10.1175/BAMS-D-12-00225.1>.

Nagura, M., and M. J. McPhaden, (2008). The dynamics of zonal current variations in the central equatorial Indian Ocean. *Geophys. Res.Lett.*, 35, L23603, [doi:10.1029/2008GL035961](https://doi.org/10.1029/2008GL035961).



Price, J. F., R. A. Weller and R. Pinkel (1986). Diurnal cycling: Observations and models of the upper ocean response to diurnal heating, cooling, and wind mixing. *Journal of Geophysical Research: Oceans*, 91, 8411-8427, doi: 10.1029/JC091iC07p08411.

Ruppert, J. H., and R. H. Johnson, (2015). Diurnally modulated cumulus moistening in the preonset stage of the Madden-Julian oscillation during DYNAMO, *Journal of the Atmospheric Sciences*, 72, 1622–1647.

Sanford, T. B., J. F. Price, and J. B. Girton, (2011). Upper-ocean response to Hurricane Frances (2004) observed by profiling EM-APEX floats. *J. Phys. Oceanogr.*, 41, 1041-1056, doi:10.1175/2010JPO4313.1.

Sanford, T. B., J. H. Dunlap, J. A. Carlson, D. C. Webb, and J. B. Girton, (2005). Autonomous velocity and density profiler: EM-APEX. *Proc. IEEE/OES Eighth Working Conf. on Current Measurement Technology, 2005*, Southampton, United Kingdom, IEEE, 152–156, doi:10.1109/CCM.2005.1506361.

Shchepetkin, A. F., and J. C. McWilliams, 2005. The regional oceanic modeling system (ROMS) a split-explicit, free-surface, topography-following-coordinate oceanic model. *Ocean Modelling*, 9, pp. 347-404.

Thorpe Stephen Austen (1977). Turbulence and mixing in a Scottish Loch *Philosophical Transactions of the Royal Society of London. Series A, Mathematical and Physical Sciences* 286:125–181. <https://doi.org/10.1098/rsta.1977.0112>.



Ushijima, Y., Yoshikawa, Y (2020). Mixed layer deepening due to wind-induced shear-driven turbulence and scaling of the deepening rate in the stratified ocean. *Ocean Dynamics* 70, 505–512. <https://doi.org/10.1007/s10236-020-01344-w>.

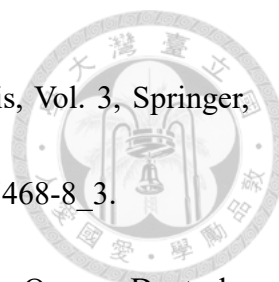
Vialard, J., G. Foltz, M. McPhaden, J.-P. Duvel, and C. de Boyer Montegut, (2008). Strong Indian Ocean sea surface temperature signals associated with the Madden-Julian oscillation in late 2007 and early 2008. *Geophys. Res. Lett.*,35, L19608, <https://doi.org/10.1029/2008GL035238>.

Vialard, J., K. Drushka, H. Bellenger, M. Lengaigne, S. Pous, and J. P. Duvel, (2013) Understanding Madden-Julian-induced sea surface temperature variations in the north western Australian Basin. *Climate Dyn.*, 41, 3203–3218, <https://doi.org/10.1007/s00382-012-1541-7>.

Wheeler, M. C. and H. H. Hendon, (2004). An all-season real-time multivariate MJO index: Development of an index for monitoring and prediction. *Mon. Wea. Rev.*, 132, 1917-1932.

Wheeler, M. C., and H. H. Hendon, (2004). An all-season real-time multivariate MJO index: Development of an index for monitoring and prediction. *Mon. Wea. Rev.*, 132, 1917–1932, [https://doi.org/10.1175/15200493\(2004\)132<1917:AARMMI>2.0.CO;2](https://doi.org/10.1175/15200493(2004)132<1917:AARMMI>2.0.CO;2).

Wyrtki, K. (1973) *Physical Oceanography of the Indian Ocean*. In: B. Zeitzschel, and



Gerlach, S.A., Eds., Ecological Studies: Analysis and Synthesis, Vol. 3, Springer, Berlin, Heidelberg, 18-36. https://doi.org/10.1007/978-3-642-65468-8_3.

Wyrski, K., (1964). The thermal structure of the eastern Pacific Ocean, Deutsche hydrographische Zeitschrift, 8, 6-84.

Yanli Jia, Kelvin J. Richards, H. Annamalai, (2021) The impact of vertical resolution in reducing biases in sea surface temperature in a tropical Pacific Ocean model, Ocean Modelling, Volume 157101722, ISSN 14635003, <https://doi.org/10.1016/j.ocemod.2020.101722>.

Zhang, C., (2005). Madden-Julian Oscillation, Reviews of Geophysics, 43, RG2003, doi:10.1029/2004RG000158.